

# Creep-plasticity-fatigue calculations in the design of porous double layers for new transpiration cooling systems

Christos G. Skamniotis and Alan C.F. Cocks

Department of Engineering Science, University of Oxford, Parks Road,  
Oxford OX7 6DP, UK

## ABSTRACT

New porous double layer (PDL) transpiration cooling technologies can allow gas turbine entry temperatures to be increased beyond current limits towards higher engine efficiency. However, PDL systems require inclined film holes with stress concentration factors in excess of 3.8. Combination of thermoelastic Finite Element (FE) analysis with Neuber type local strain approaches gives similar cyclic strain range predictions with cyclic plasticity-creep FE analysis. Fatigue crack initiation at film holes occurs with a low number of cycles due to excessive plasticity. Our study establishes links between elastic-inelastic analyses and between material phenomena-PDL geometry and indicates pathways of improving life.

**Keywords:** transpiration cooling, film cooling holes, creep-plasticity-fatigue, thermo-mechanical fatigue, Neuber's rule.

## Nomenclature

### Abbreviations

PDL = porous double layers  
FE = Finite elements  
2D = two-dimensional  
3D = three-dimensional  
SCF = stress concentration factor  
MPC = multipoint constraint  
UDISP = user defined displacement (ABAQUS subroutine)

### Symbols

#### Thermal

$T_{max}$  = temperature at hot surface of hot layer (°C)  
 $T_{min}$  = minimum temperature at inner surfaces (°C)  
 $T_0$  = room temperature (°C)  
 $T_o$  = reference temperature for creep law (°C)  
 $\Delta T$  = thermal difference (°C)

#### Structural

$b_1$  = outer layer thickness (mm)  
 $b_2$  = outer layer thickness (mm)  
 $\gamma$  = film hole inclination (°)  
 $G$  = geometric parameter  
 $R$  = radius of curvature (mm)

$L$  = pedestal spacing (mm)  
 $H$  = pedestal height (mm)  
 $D_P$  = pedestal diameter (mm)  
 $D_O$  = film hole diameter (mm)  
 $\rho_O$  = film hole fillet radius (mm)  
 $D_{O_{imp}}$  = impingement hole diameter (mm)  
 $\rho_{O_{imp}}$  = impingement hole fillet radius (mm)

#### Material

$E$  = Elastic Modulus (MPa)  
 $\nu$  = Poisson's ratio  
 $\alpha$  = thermal expansion coefficient (1/K)  
 $k$  = thermal conductivity (W/(m·K))  
 $Q$  = activation energy (kJ/mol)  
 $\dot{\epsilon}_0$  = reference creep rate (1/h)  
 $\sigma_0$  = reference stress for creep law (MPa)  
 $n$  = creep power law exponent  
 $\sigma_{y_T}$  = temperature dependent yield stress (MPa)  
 $\sigma_{y_0}$  = yield stress at room temperature (MPa)  
 $R$  = universal gas constant (J/mol·K)

#### Mechanical

$\kappa$  = total bending curvature (mm<sup>-1</sup>)  
 $I$  = second moment of area (mm<sup>4</sup>)  
 $\epsilon_{ep}$  = elastoplastic strain  
 $\epsilon_p$  = plastic strain  
 $\epsilon_{cr}$  = creep strain  
 $\epsilon_{creq}$  = equivalent creep strain  
 $\epsilon_e$  = elastic strain  
 $\epsilon_{cr_z}$  = additional creep strain between  $Z > 1$  and  $Z = 1$  cases  
 $\epsilon_{in}$  = inelastic strain (plastic plus creep)  
 $\epsilon_{p_{cooldown}}$  = plastic strain on cool-down  
 $\epsilon_{peq_{cooldown}}$  = equivalent plastic strain on cool-down  
 $\epsilon_{p_{heatup}}$  = plastic strain on heat-up  
 $\Delta\epsilon$  = total strain range  
 $E_{e_{Neuber}}$  = elastic strain and complementary energy density (mJ/mm<sup>3</sup>)  
 $E_{e_{Molski-Glinka}}$  = elastic strain energy density (mJ/mm<sup>3</sup>)  
 $N$  = membrane force per unit length (N/mm)  
 $M$  = bending moment per unit length (N·mm/mm)  
 $G$  = increase of stress in hot layer due to the presence of the inner layer  
 $Z$  = elastic follow-up factor  
 $\sigma$  = maximum absolute principal (Cauchy) stress (MPa)  
 $S$  = thermoelastic (compressive) stress magnitude (MPa)  
 $\sigma_j$  = (Cauchy) stress component in  $j$  direction (MPa)

$\sigma_{max}$  = maximum principal stress (MPa)

$\sigma_{med}$  = medium principal stress (MPa)

$\sigma_{min}$  = minimum principal stress (MPa)

$\sigma_{eq}$  = equivalent stress (MPa)

Time

$dt$  = time increment (h)

$t_{trans}$  = heat-up and cool-down time periods (h)

$t_{dwell}$  = high temperature/creep dwell time period (h)

$t_{rest}$  = rest period (h)

Fatigue

$N_f$  = cycles to failure (fatigue crack initiation)

$\tau, C$  = temperature dependence parameters for fatigue

$A_1, A_2, B_1, B_2$  = fatigue curve constants

## Accents – superscripts

$\hat{\phantom{x}}$  = quantity normalised over outer wall thickness (dimensionless)

$\bar{\phantom{x}}$  = dimensionless position

## Subscripts

1 = outer (hot) layer property

2 = inner (cooler) layer property

$y$  = position through layer thickness (mm)

$\theta$  = circumferential axis/direction

$z$  = longitudinal axis/direction

$r$  = radial axis/direction

$x$  = x direction

$y$  = y direction

$z$  = z direction

# 1. Introduction

Turbine efficiency is key for various power plant and transport applications, with direct benefits to the broader economy and society [3]. For example, more efficient turbines will reduce carbon dioxide emissions [4] and lower air ticket prices whilst eventually allowing hypersonic civil travel at lower launch costs. Advances in jet engines have largely relied on the principle that higher gas core temperatures leads to higher thermodynamic cycle efficiency [5, 6]. As a result, turbine gas temperatures have risen by 500 °C over the last fifty years [7, 8]. This has been possible through continuously improving cooling technologies, with the contributions of metal alloys, thermal barrier coatings and manufacturing being less significant [5, 9]. As current metallic engine parts are immersed in gas flow temperatures of 2000 °C [10], significantly in excess of their melting point, research on revolutionary cooling systems is required to push the boundaries further.

The porous double layer (PDL) system shown in Fig 1a for a turbine blade, is one such innovation that promises outstanding cooling and thermal protection functionalities [11]. This owes to a combination of external film holes through an outer (hot) layer and internal impingement holes through an inner (cool) layer. The impingement holes eject cool air against the interior of the hot

layer, whereas the film holes aid in forming a protective heat shield against the hot gas. The substantial benefit is that internal air flow occurs in a turbulent manner, taking up larger amounts of heat than any current transpiration cooling system [12, 13]. Heat conduction through pedestals is also suggested to reduce thermal gradients and overall temperatures in the outer layer. Computational Fluid Dynamics (CFD) models have indicated that benefits from the outstanding convective efficiency and cooling effectiveness of PDLs can outweigh the efficiency penalty related to aerodynamics and coolant volume supply [12]. A major challenge in integrating PDLs into real turbine components is to address specific life requirements despite the stress raising effects near holes and sharp pedestal corners [14]. The unknown severity of thermal stresses associated with the potentially large temperature differences between the two layers, has hindered the life assessment of the new systems [15].

Current knowledge in the mechanics of PDL systems is limited to a few studies in the elastic regime [14-17]. Most of them have used axisymmetric and 2D idealisations to understand the complexity of the thermal stress field in the new double layer architecture without holes [16, 17]. Recently, the authors advanced the analysis to more detailed 3D geometries [14]; a key finding was that PDLs self-impose significant kinematic constraints such that a temperature difference between the two layers causes significant thermal stresses. These nominal stresses are magnified near impingement/film holes and connecting pedestals, represented in terms of a stress concentration factors, SCF, with the inclined film holes displaying the most severe SCF values [14].

In reality, the extreme thermoelastic stress magnitudes at film holes cannot be contained within yield, suggesting that significant plastic deformation occurs and a residual stress profile is developed upon temperature removal [18, 19]. This cyclic/alternating plasticity process eventually results in low cycle thermal fatigue failure, particularly at critical regions of film holes with large inclinations,  $\gamma$  [20, 21]. At the same time, inclined film holes are necessary for preventing the mixing of the coolant with the mainstream hot gas flow as well as for producing a complete protective film at the critical external hot surface [6, 22]. The above suggest that a fatigue assessment is necessary in order to design PDL systems that minimise both the heat flux into the material and the thermal stresses [4]. For this reason, our study presented here develops, for the first time, a creep-plasticity-fatigue evaluation for inclined hole geometries in double layer systems.

We derive theoretical-FE solutions for the critical thermoelastic stress range at film holes and then use a local strain approach based on Neuber [23] and Molski-Glinka [24] schemes to calculate analytically the critical inelastic strain range responsible for fatigue failure [25, 26]. A local strain approach is an essential step towards understanding the role of various geometric, thermal loading and material parameters of the new PDL systems, in the creep-fatigue failure processes. Simplified failure assessment methods of this type have proven popular in aerospace design in obtaining conservative life predictions [27, 28]. Such predictions can immediately narrow the range of conditions for which more elaborate analyses need to be performed. Our results will therefore enable useful comparisons against more elaborate predictions of the structural cyclic state under non-local considerations [29], which will eventually answer important questions, e.g. what is the required level of sophistication in design codes for PDL systems and whether simplified conservative approaches limit innovation.

In Section 2 we describe the geometry and thermal loading cycle characteristics of the system, followed by a description of the constitutive law we use here for the CMSX-4 alloy. Section 3 presents thermoelastic stress solutions, the inelastic analysis and the fatigue evaluation scheme. Section 4 describes our FE results on inelastic cycle-by-cycle simulations, followed by fatigue life predictions, discussion and concluding remarks.

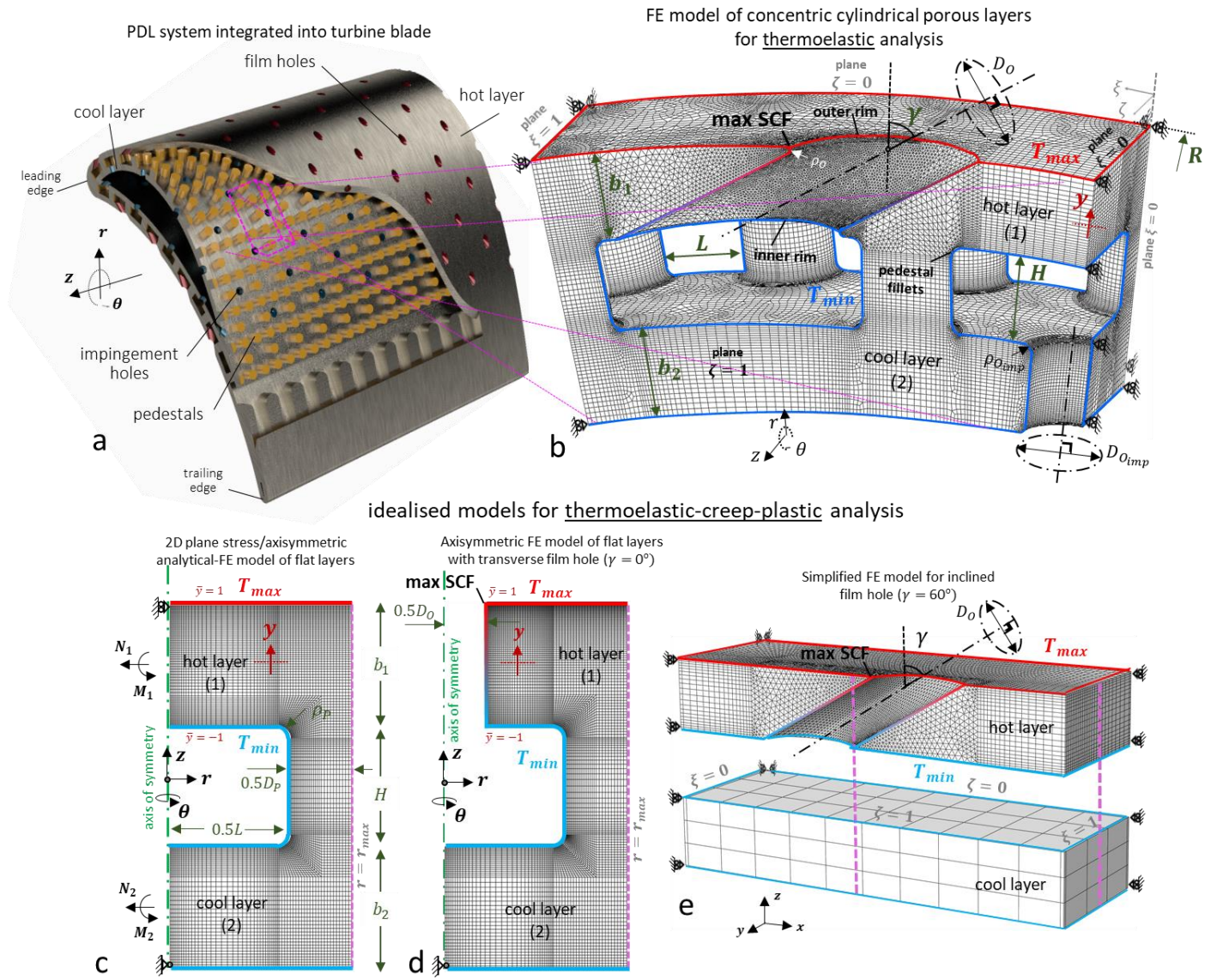


Figure 1. (a) Porous double layer (PDL) cooling system implemented in a turbine blade. (b) repeating unit cell of PDL system used in the FE thermoelastic analysis to determine the maximum SCF at the acute wedge of the outer rim of the film hole. (c) Simplified 2D plane strain stress/axisymmetric FE model of flat double layers. (d) axisymmetric FE model used for inelastic analysis of a transverse hole ( $\gamma = 0^\circ$ ). (e) double plate FE model used for inelastic analysis of an inclined film hole ( $\gamma = 60^\circ$ ).

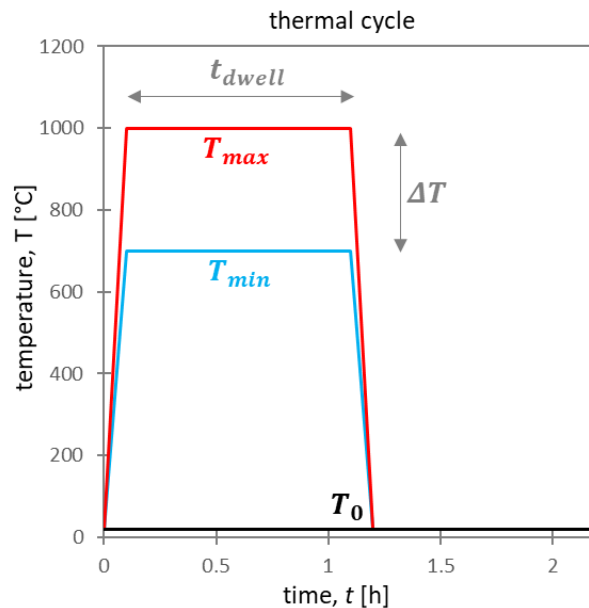


Figure 2. (a) Typical thermal cycle used in FE analysis and local strain approach.

## 2. Materials and Methods

### 2.1 Porous double layer geometries and kinematic constraints

Idealising a double layer blade (Fig 1a) of varying curvature by cylindrical double layers of constant curvature was shown to be a valid approach for capturing the thermoelastic stress field that arises in particular regions of the blade in [16]. This is because both of the above cases involve a closed cross-sectional profile, such that the main kinematic constraint is the same – i.e. the rotations of the layers about  $\theta$  and  $z$  axes during thermal loading are zero. This is based on the assumption that the thermal gradients through the layer thicknesses are constant throughout the configuration. We take advantage of the above characteristic to model the system in Fig 1a via the repeating block in Fig 1b, which represents long concentric cylindrical porous layers. Since for thin layer structures, i.e.  $R/b_1 > 20$ , the geometric curvature does not play a major role in the thermoelastic stress field [15], material creep-plasticity under thermal cycling is investigated by the flat simplified models in Figs 1c-e. The model in Fig 1c is used to understand the inelastic response in the absence of holes under plane stress/axisymmetric conditions. We then explore effects in the presence of transverse holes ( $\gamma = 0^\circ$ ) and inclined holes ( $\gamma = 60^\circ$ ) through the models in Fig 1d and Fig 1e, respectively. Geometric features in Figs 1b-e of unity length include the hot layer thickness,  $b_1$ , cool layer thickness,  $b_2$ , pedestal height,  $H$ , pedestal spacing,  $L$  and pedestal diameter,  $D_p$ ; impingement and film hole diameters,  $D_{o_{imp}} = D_o = 0.7b_1$ , and corresponding fillet radii,  $\rho_{o_{imp}} = \rho_o = 0.1b_1$  (Fig 1b), are also used.

The FE mesh in Figs 1b-e, mainly consist of 8-node hexahedral elements and 4-node tetrahedral elements near inclined holes (Figs 1b,e). The mesh density is chosen based on a preliminary mesh sensitivity analysis which ensures that both the thermoelastic and inelastic stress-strain results in the vicinity of the acute wedge of the film hole (denoted as max SCF in Fig 1b) do not change with further mesh refinement. For the inelastic range, this requires that at least 5-6 elements undergo plasticity in the vicinity of the acute wedge of the film hole (Fig 1b,e), even at low levels of thermal loading.

Symmetry boundary conditions are applied in Fig 1b at planes,  $\xi = 0$ ,  $\xi = 1$  ( $u_\theta = 0$ ) and  $\zeta = 0$  ( $u_z = 0$ ), while all the nodes at  $\zeta = 1$  must satisfy common  $u_z$  displacement; symmetry at  $\xi = 0$ ,  $\xi = 1$  has been found to yield approximately the same results with periodic boundary (cyclic symmetry) conditions for the geometry of Fig 1b [14]. The relevance of all the above boundary conditions to the case of long cylindrical double layers and the case of double layer turbine blade has been studied extensively in [16]. These conditions imply that in Fig 1b the rotations of the layers about  $\theta$  and  $z$  axes are zero and that the thermoelastic extension of the layers along the  $z$  direction is common. The additional models used here (Figs 1c-e) mimic the above conditions. For example, in Fig 1e the pink symmetry lines are enforced to remain straight i.e. the walls extend by the same amount along the  $y$  axis, as well as along the  $x$  axis. This also requires the symmetry conditions  $u_x = 0$  and  $u_y = 0$  at planes  $\xi = 0$  and  $\zeta = 0$ , respectively. In the same manner, in Figs 1c-d we postulate that  $u_r = 0$  at all nodes for which  $r = 0$  and common  $u_r$  for nodes lying at  $r = r_{max}$ . We use the commercial FE software ABAQUS [30] to perform transient temperature-displacement analysis based on the Newton-Raphson scheme. The above kinematic constraints and the temperature field in Figs 1b,e are applied through the ABAQUS MPC and UDISP subroutines [30], respectively.

### 2.2 Thermal loading of porous double layers

The temperature field used in Figs 1b-e is based on the steady state temperature field for the PDL system obtained in [31] using conjugate CFD-heat transfer analysis; the characteristics of these solutions have been discussed in detail elsewhere [17]. The temperature field generally involves a thermal gradient,  $\Delta T = (T_{max} - T_{min})/b_1$ , through the hot (outer) layer thickness,  $b_1$  (see Fig 1b),

a thermal gradient through the pedestal height and an effectively uniform temperature in the cool (inner) layer. Here we assume that  $T_{max}$  is constant along the hot outer surface and that  $T_{min}$  occurs uniformly at the interior surfaces of the system (see Fig 1b), such that  $\Delta T$  is constant along the plane of the hot layer. In practise,  $T_{max}$  varies throughout the hot outer surface and the thermal gradient through the height of the pedestals is significant [31], such that a non-uniform temperature profile exists throughout the interior of the system. The significance of these additional features on the integrity of the system is explored in a later study [32]. Describing thermal loading by the two parameters,  $T_{max}$  and  $\Delta T$  (or  $T_{min}$ ), is found to be instructive when evaluating the inelastic behaviour and fatigue performance, particularly given that the PDL system has not been studied inelastically before. The same idealisation strategy has been adopted in [15-17] in order to provide a clear understanding of the thermoelastic response of this new type of thermal protection system.

The thermal cycle which we will use here based on the above temperature field idealisation is shown in Fig 2. The system is originally at a uniform ambient temperature,  $T_o = 20$  °C. The temperatures,  $T_{max}$ ,  $T_{min}$  are then ramped up at constant rates with time to the hot state, such that within a transient time period,  $t_{trans} = 0.1$  h, they obtain their maximum values; this part of the cycle is referred to as the ‘heat-up’ process. This temperature distribution is maintained for a steady state time period,  $t_{dwell} = 1$  h, also referred to as a ‘dwell’ period, before the  $T_{max}$  and  $T_{min}$  temperatures are ramped down at the same rates as during the heat-up period, such that within a time period,  $t_{trans}$ , they return to the ambient temperature,  $T_o$ ; this drop in temperatures will be referred to as ‘cooldown’. The exact time period during which ambient conditions are then maintained,  $t_{rest} = 1$  h, (rest period) does not play a role in the results, based on the temperature boundary conditions and the thermal conductivity used here. In this study we consider fixed values of  $t_{trans}$ ,  $t_{dwell}$  and  $t_{rest}$  and instead vary the  $T_{max}$  and  $\Delta T = (T_{max} - T_{min})$  parameters. Mechanical loading is ignored here; a relevant discussion is provided at the end of Section 5.

## 2.3 Material constitutive law

The material constitutive behaviour can be idealised (in one dimension) for small strains by the addition of thermal, elastic, plastic and creep strains, giving a total strain increment:

$$d\varepsilon = d\varepsilon_T + d\varepsilon_e + d\varepsilon_p + d\varepsilon_{cr} \quad (1)$$

where  $d\varepsilon_T = \alpha dT$  is the thermal strain increment for temperature change,  $dT$ ,  $d\varepsilon_e = d\sigma/E$ , is the elastic strain increment due to a stress increment,  $d\sigma$ , for a material with elastic modulus,  $E$ ,  $d\varepsilon_p$  is the plastic strain increment and  $d\varepsilon_{cr}$  is the creep strain increment defined by the power law:

$$d\varepsilon_{cr} = dt \dot{\varepsilon}_o \left( \frac{|\sigma|}{\sigma_o} \right)^n \text{sgn}(\sigma) \exp(x) \quad (2)$$

where  $x = -\frac{Q}{R} \left( \frac{1}{T} - \frac{1}{T_o} \right)$ , and  $dt$  is the time increment.  $\sigma$  and  $T$  are the current stress and temperature,  $\dot{\varepsilon}_o$ ,  $\sigma_o$ ,  $T_o$  are the three constants defining the constant creep strain rate under a constant (reference) stress and temperature,  $n$  is the creep exponent,  $Q$  is the activation energy,  $R = 8.31$  J/(mol·K) is the universal gas constant and  $\text{sgn}(\sigma)$  is the sign of  $\sigma$ . In Eq (2) it is ensured that  $|\sigma| \leq \sigma_{y_T}$ , where  $\sigma_{y_T}$  is the temperature dependent yield stress, which is assumed to remain constant with plastic straining i.e. perfect plasticity, and to be independent of pressure i.e. same in compression and tension. In FE calculations, the behaviour is implemented based on a von Mises yield surface; in this case Eq (2) relates the equivalent creep strain increment to the equivalent stress,  $\sigma$ .

The material model is calibrated based on the yield strength versus temperature data (Fig 3a) and isothermal creep rate versus constant stress data (Fig 3b) reported in [1] and [2] respectively, for the CMSX-4 nickel superalloy. This yields the creep parameters,  $\dot{\varepsilon}_o = 1/\text{h}$ ,  $\sigma_o = 800$  MPa,  $T_o = 830$  °C,



$Q = 400$  kJ/mol,  $n = 10$ , and the room temperature yield stress,  $\sigma_{y_0} = 805$  MPa. The elastic and thermal properties are assumed to be temperature independent and the values reported in [33] for 700 °C are used, including the Young's Modulus,  $E = 100$  MPa, Poisson's ratio,  $\nu = 0.4$ , thermal expansion coefficient,  $\alpha = 17.4 \cdot 10^{-6}$  1/K and thermal conductivity,  $k = 19.4$  W/(m·K). All the parameters used for CMSX-4 here correspond to the  $\langle 001 \rangle$  crystallographic orientation.

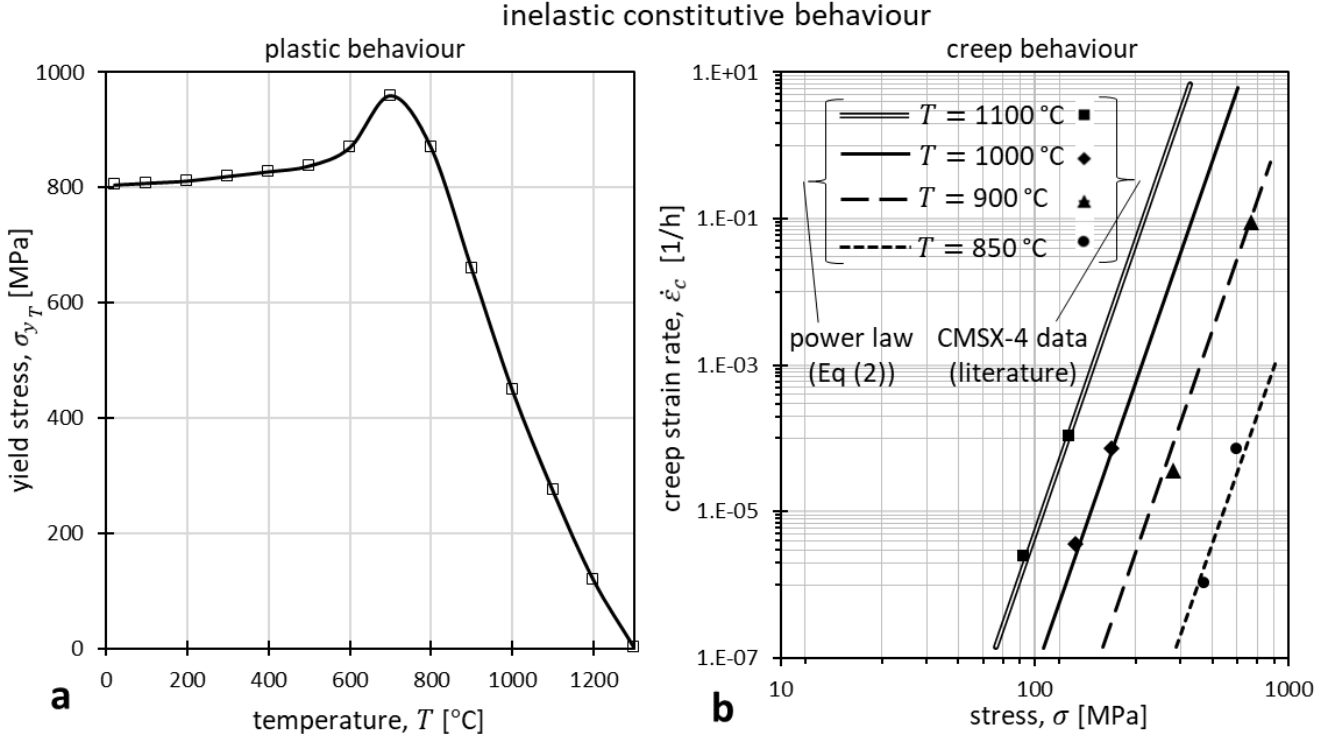


Figure 3. Inelastic behaviour of CMSX-4 nickel alloy used for inelastic analysis. (a) Temperature dependence of yield stress (reproduced from [1]), (b) calibration of power creep law to match isothermal data of creep rate versus constant stress presented in [2].

## 3 Calculations

### 3.1 Theoretical thermoelastic solution

Theoretical thermoelastic solutions for the geometries shown in Fig 1 are given in [15, 16]; more detailed FE solutions are available in [14]. We demonstrate in these papers how the general stress states within the transpiration cooling system represented by Fig 1b can be determined analytically using beam and plate theory and how these are modified at features, such as impingement and film holes. We provide an overview of the main results here. This serves to illustrate three important aspects of these results that are relevant to the current paper. It:

- justifies the relevance between the simplified models in Figs 1c-e and the real system in Fig 1b,
- provides the basis for subsequent theoretical analysis in the inelastic regime,
- leads to analytical expressions for the critical thermoelastic stress at the film hole (denoted by max stress concentration factor (SCF) in Fig 1b), which can be used in a local failure approach.

Regardless of the presence of film holes, the primary feature in the long cylindrical geometries represented by the unit block of Fig 1b, is that the thermal curvature,  $\kappa_T = \Delta T/b_1$ , in the hot layer is self-constrained by the kinematics of the overall geometry, i.e. no rotations are allowed [16]. Secondly, the pedestals prevent the two layers from moving apart, implying that the layers must



extend equally along  $\theta$  and  $z$  directions (see Fig 1b). The above two conditions, along with force equilibrium lead to:

$$\begin{aligned} \kappa_1 = \kappa_{1_e} + \kappa_{1_T} = 0 &\rightarrow \frac{M_1}{EI_1} + \frac{a\Delta T}{b_1} = 0 \quad (i) \\ \bar{\varepsilon}_1 = \bar{\varepsilon}_2 &\rightarrow \bar{\varepsilon}_{1_e} + \bar{\varepsilon}_{1_T} = \bar{\varepsilon}_{2_e} \rightarrow \frac{N_1}{Eb_1} + \frac{a\Delta T}{2} = \frac{N_2}{Eb_2} \quad (ii) \\ N_1 + N_2 &= 0 \quad (iii) \end{aligned} \tag{3}$$

where  $\kappa_1$  is the total bending curvature in the hot layer, corresponding to the second moment of area per unit length,  $I_1 = b_1^3/12$ , and bending moment,  $M_1$ , and  $\bar{\varepsilon}_1, \bar{\varepsilon}_2$  are the total membrane strains in the two layers corresponding to the membrane forces,  $N_1, N_2$ ; note that  $I_1, M_1, N_1, N_2$  are per unit length. Eqs (3) apply in both principal directions,  $\theta$  and  $z$  of the cylindrical system in Fig 1b and the current analysis based on classical/flat plate theory is valid for sufficiently thin layers i.e.  $R \gg b_1$  and narrow pedestal spacing i.e.  $R \gg L$  [16]; if the latter is not satisfied then the moments/forces in each layer can vary with position with respect to the pedestal [16]. Also note that Eq (3ii) is valid for the  $\theta$  direction when the external radius of curvature and pedestal height satisfy  $R \gg H$ . All the above conditions are satisfied in Fig 1b. Application of Eqs (3) along the  $\theta$  and  $z$  axes together with Hooke's law, produces a system of equations that is solved to give the following nominal thermoelastic stress (in the absence of film holes) as a function of position,  $y$ , through the hot layer thickness :

$$\sigma(y) = \frac{N_1}{b_1} + \frac{M_1 y}{I_1} = - \left[ \frac{b_2}{2(b_1 + b_2)} + \frac{1}{b_1} y \right] \frac{Ea\Delta T}{(1 - \nu)} \tag{4}$$

By using  $y = b_1/2$  in Eq (4) and adding the maximum (max) SCF associated with the presence of the film hole, we finally determine the peak compressive stress magnitude (also referred to as thermoelastic stress range and/or fictitious elastic stress range) in Fig 1b as:

$$S = \text{SCF} \frac{Ea\Delta T}{(1 - \nu)} G \tag{5}$$

where  $G = (0.5 + b_2/b_1)/(1 + b_2/b_1)$  is a monotonic function of the layer thickness ratio,  $b_2/b_1$ , and SCF is the ratio of the actual stress in the vicinity of the acute wedge of the film hole, determined from detailed finite element (FE) calculations and denoted as max SCF in Fig 1b, normalised over the corresponding nominal stress in the absence of the hole. Note that the analytical result gives the influence of global geometric parameters and the effect of local geometry is captured through the SCF. The dependence of the max SCF of Fig 1b for the film hole on the relative size, shape and orientation of the hole is given in [14].

## 3.2 Theoretical inelastic solution

### 3.2.1 Global considerations

We now extend the governing thermoelastic analysis (Eqs (3)) to determine how the nature of the solution changes with creep-plastic deformation. Considering the system without holes in Fig 1c, stress relaxation due to creep in the hot layer (no creep in the cool layer) must always satisfy:

$$\int_{-\frac{b_1}{2}}^{\frac{b_1}{2}} d\sigma y dy - dM_1 = 0 \quad (i)$$

$$\int_{-\frac{b_1}{2}}^{\frac{b_1}{2}} d\sigma dy - dN_1 = 0 \quad (ii)$$
(6)

in which, by using Eqs (1,2) ( $d\varepsilon_p = 0$ ) and classical beam/plate theory i.e.  $d\varepsilon = d\kappa_1 y + d\bar{\varepsilon}_1$ , the stress increment,  $d\sigma$ , at position,  $y$ , through the hot layer thickness, after a time  $dt$ , during which the temperature changes by an amount  $dT$ , is:

$$d\sigma = E d\varepsilon_e = E \left[ d\kappa_1 y + d\bar{\varepsilon}_1 - a dT - dt \dot{\varepsilon}_o \left( \frac{|\sigma_t|}{\sigma_o} \right)^n \exp(x) \right] \quad (7)$$

where  $\sigma_t$  refers to the stress at the end of the previous increment. Substitution of Eq (7) into Eq (6i) and integration over the hot layer thickness,  $b_1$ , gives the total curvature increment,  $d\kappa_1$ , and substitution of Eq (7) into Eq (6ii) and integration gives the total membrane strain increment,  $d\bar{\varepsilon}_1$ . We then obtain:

$$d\kappa_1 = \frac{dM_1}{EI_1} + a \frac{dT}{b_1} + \frac{1}{I_1} \int_{-\frac{b_1}{2}}^{\frac{b_1}{2}} \left[ dt \dot{\varepsilon}_o \left( \frac{|\sigma_t|}{\sigma_o} \right)^n \exp(x) y \right] dy = 0 \quad (i)$$

$$d\bar{\varepsilon}_1 = \frac{dN_1}{Eb_1} + a \frac{dT}{2} + \frac{1}{b_1} \int_{-\frac{b_1}{2}}^{\frac{b_1}{2}} \left[ dt \dot{\varepsilon}_o \left( \frac{|\sigma_t|}{\sigma_o} \right)^n \exp(x) \right] dy = d\bar{\varepsilon}_2 = \frac{dN_2}{Eb_2} \quad (ii)$$

$$dN_1 + dN_2 = 0 \quad (iii)$$
(8)

in which use has been made of the kinematic requirements of zero total curvature (since  $\kappa_1 = 0$  in Eq (3i), and also  $d\kappa_1 = 0$  in Eq (8i)); equal membrane strains in the two layers (since  $\bar{\varepsilon}_1 = \bar{\varepsilon}_2$  in Eq (3ii), and also  $d\bar{\varepsilon}_1 = d\bar{\varepsilon}_2$  in Eq (8ii)); and the equilibrium of membrane forces (Eq (8iii)). In this manner, we have extended the 3x3 system of Eqs (3) for the thermoelastic response into the incremental form of Eqs (8) for the thermoelastic-creep response. The term  $d\Delta T = (T_{max_{t+dt}} - T_{min_{t+dt}}) - (T_{max_t} - T_{min_t})$  is the increment in the thermal gradient during the time increment. The bending moment and membrane force increments,  $dM_1$ ,  $dN_1$  and  $dN_2$ , can be found analytically for each time step,  $dt$ , by calculating the integrals associated with the creep curvature increment,  $d\kappa_{1_{cr}}$ , in Eq (8i) and creep membrane strain increment,  $d\bar{\varepsilon}_{1_{cr}}$ , in Eq (8ii) (e.g. via a trapezoidal method) based on the known stress distribution,  $\sigma_t = \sigma_t(y)$ , at the end of the previous step.  $dM_1$ ,  $dN_1$  can then be fed into Eq (7) to find the stress increment,  $d\sigma$ , for each position,  $y$ , in the hot layer and the stress,  $\sigma_{t+dt} = \sigma_t + d\sigma$ , at the end of the increment. If yield is violated i.e.  $|\sigma_{t+dt}| > \sigma_{y_T}$ , plasticity is taken into account by using  $\sigma_{t+dt} = \sigma_{y_T}$  and reducing the elastic increments.

The above Euler-explicit scheme provides results in close agreement with 2D plane stress FE results from Fig 1c (not shown). This adds credibility to Eqs (8) for describing the evolution of the nominal stress distribution in double wall systems. Similar to the elastic analysis this calculation

serves to provide insights into how global features, e.g. the layer thickness ratio,  $b_2/b_1$ , influences the evolution of stress during a thermal cycle [20], as well as providing a framework for interpreting the inelastic FE results.

### 3.2.2 Local considerations

A major objective of the global inelastic analysis is to determine the local strain range,  $\Delta\epsilon$ , at the critical film hole location, which is the necessary input parameter for predicting fatigue life [8]. For this we employ cycle-by-cycle inelastic FE analysis as well as an analytical local strain approach [34]. Implementation of the above methods firstly requires considering the type of inelastic strain cycle at the critical film hole location, based on the thermal cycle described earlier in Section 2.2 and illustrated in Fig 2. Fig 4a depicts an idealised inelastic cycle for a uniaxial stress state based on the initial assumption that the cycle saturates after one cycle and that plastic deformation occurs at the extremes of the cycle when the temperature dependent yield stress,  $\sigma_{yT}$ , either equals the ambient value,  $\sigma_{y0}$ , or the value at the maximum temperature,  $\sigma_{yT_{max}}$ . Under this assumption, the following characteristic features can be identified in Fig 4a:

1. Onset of yield during the first heat-up (first cycle) at a compressive stress,  $\sigma_1 = -\sigma_{yT_{max}}$ .
2. End of first heat-up at the same stress,  $\sigma_2 = -\sigma_{yT_{max}}$ , and corresponding compressive elastoplastic (total) strain,  $\epsilon_2 = -\epsilon_{ep02}$ .
3. End of creep dwell at a relaxed stress,  $\sigma_3 < 0$ , and corresponding total strain,  $\epsilon_3 = \epsilon_2 + \epsilon_{cr} + \epsilon_{e23}$ , where  $\epsilon_{cr}$  is the creep strain accumulation during the creep dwell period (here  $\epsilon_{cr} < 0$ ), and  $\epsilon_{e23} = (\sigma_2 - \sigma_3)/E$  is the associated reduction of the elastic strain (here  $\epsilon_{e23} < 0$ ).
4. Onset of yield during cool-down at a tensile (residual) stress,  $\sigma_4 = \sigma_{y0}$ .
5. End of cool-down at the same residual stress,  $\sigma_5 = \sigma_{y0}$ , and total strain  $\epsilon_5 = \epsilon_3 + \epsilon_{ep35}$ , where  $\epsilon_{ep35}$  is the absolute elastoplastic strain change from point 3 to point 5, corresponding to a plastic strain growth,  $\epsilon_{p_{cooldown}}$ .
6. Onset of yield during subsequent heat-up at a compressive stress,  $\sigma_6 = -\sigma_{yT_{max}}$ .
7. End of subsequent heat-up (for a closed cycle), at stress,  $\sigma_7 = -\sigma_{yT_{max}}$ , and total strain,  $\epsilon_7 = \epsilon_5 - \epsilon_{ep52}$ , where  $\epsilon_{ep52}$  is the absolute elastoplastic strain change from point 5 to point 2, corresponding to an absolute plastic strain growth,  $\epsilon_{p_{heatup}}$ .

In practice, a cyclic state in which the cyclic response does not vary from one cycle to the next, will be achieved after a number of cycles. As a result, in reality, the end of a subsequent heat-up will not correspond to point 2 but instead to point 7 (and the end of the subsequent creep dwell to point 8 instead of point 3) – see Fig 4a; note that point 7 may generally correspond to a larger or smaller total compressive strain than point 2. Here, however, we assume that the cyclic state is achieved after point 5, both in terms of stresses and cyclic inelastic strains. As a result, the end of subsequent heat-ups, i.e. point 7, will coincide with point 2 and the above loop continues with further cycling. In this case, Fig 4a indicates that the absolute compressive inelastic strain growth at high temperature,  $\epsilon_{cr} + \epsilon_{p_{heatup}}$ , is equal to the tensile inelastic strain growth at ambient temperature,  $\epsilon_{p_{cooldown}}$ . The same applies when thermal loading is less severe than in Fig 4a, i.e. when  $\epsilon_{p_{heatup}} = 0$ , such that point 6 coincides with point 2 and therefore  $\epsilon_{cr}$  is equal to  $\epsilon_{p_{cooldown}}$ . In more detail, assuming that ratcheting does not occur, the possible regimes of local inelastic behaviour can be found by

comparing the thermoelastic stress range,  $S$  in Fig 4a, against the yield strengths  $\sigma_{y_0}$  and  $\sigma_{y_{T_{max}}}$ , as follows:

- I. When  $S \leq \sigma_{y_0}$ , compressive plastic straining can occur during the first heat-up (since  $\sigma_{y_{T_{max}}} < \sigma_{y_0}$ ) but the residual tensile stress on cool-down will never violate yield. As a result, the residual tensile stress will gradually increase with further cycling due to the accumulation of creep strain,  $\varepsilon_{cr}$ , during the creep dwell (high temperature) periods of the cycles and the associated relaxation of the compressive stress. This process will continue until the compressive stress relaxes completely to zero and the tensile residual stress becomes constant, i.e. complete elastic shakedown (locally).
- II. When  $\sigma_{y_0} < S \leq \sigma_{y_0} + \sigma_{y_{T_{max}}}$ , after a number of creep dwells the accumulated creep strain,  $\varepsilon_{cr}$ , will become large enough to cause the tensile stress on cooldown to reach yield, i.e. tensile plastic straining,  $\varepsilon_{p_{cooldown}}$ , will then occur during cooldown. During subsequent cycles, the creep strain accumulated at high temperature will be equal and opposite to the plastic strain at low temperature, i.e.  $\varepsilon_{cr} = \varepsilon_{p_{cooldown}}$ . This is often referred to as plastic shakedown.
- III. When  $S > \sigma_{y_0} + \sigma_{y_{T_{max}}}$ , the thermoelastic stress range cannot be contained within yield, such that plastic straining occurs both during heat-up and cooldown from the very first cycle. The relationship between inelastic strains for regime II now becomes,  $\varepsilon_{cr} + \varepsilon_{p_{heatup}} = \varepsilon_{p_{cooldown}}$ , which is the case in Fig 4a.

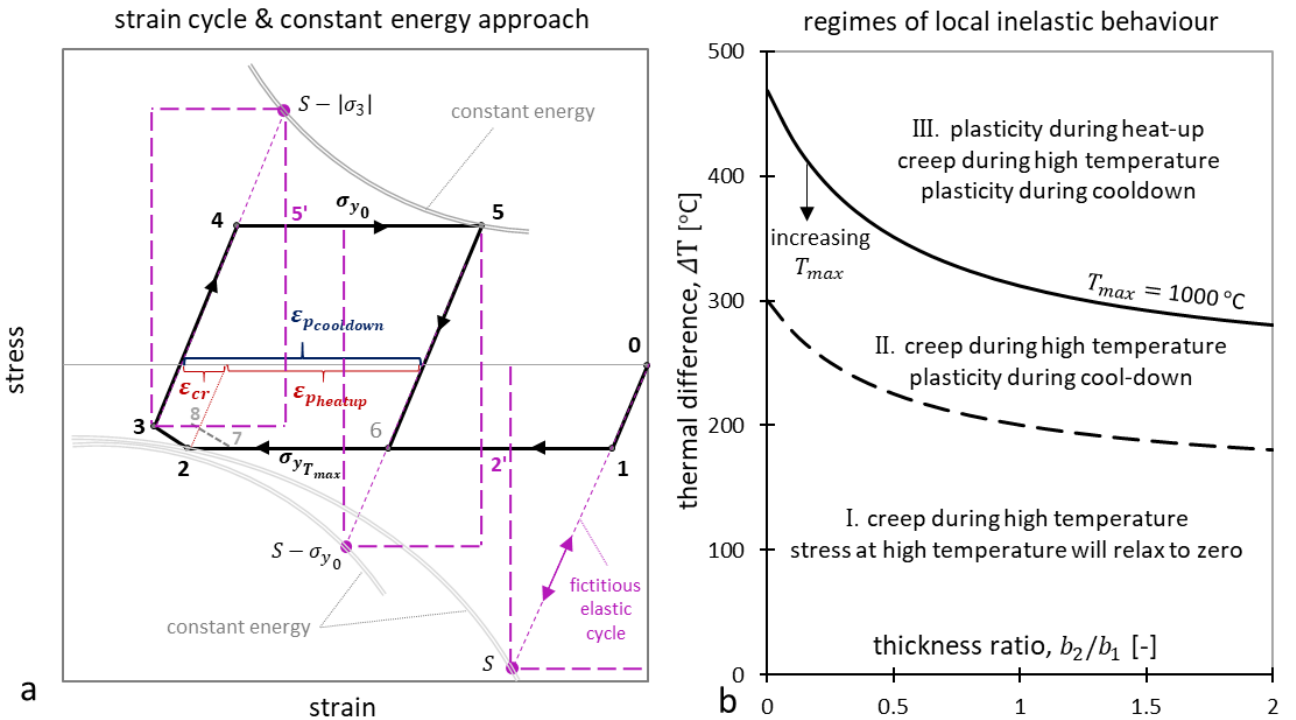


Figure 4. (a) Idealised inelastic cycle for the critical location of the film hole together with fictitious elastic predictions. (b) Regimes of local inelastic behaviour as a function of thermal difference,  $\Delta T$ , and layer thickness ratio,  $b_2/b_1$ .

Fig 4b illustrates these three regimes of behaviour I-III for the critical film hole location as a function of thermal difference,  $\Delta T$ , through the hot layer and the layer thickness ratio,  $b_2/b_1$ . The

boundary between regimes I-II is found by replacing  $S$  in Eq (5) with  $\sigma_{y_{T_{max}}}$ , whereas for the II-III boundary we replace  $S$  with  $\sigma_{y_0} + \sigma_{y_{T_{max}}}$ . Since  $\sigma_{y_{T_{max}}}$  in the CMSX-4 alloy decreases with temperature above 800 °C (Fig 3a), increasing  $T_{max}$  translates the II-III boundary downwards (Fig 4b).

Here we are interested in regimes II-III, and by using an analytical local strain approach we calculate the total strain range,  $\Delta\epsilon$ , bounded between the total strains at points 3 and 5 in Fig 4a, solely based on information from an elastic analysis, i.e. the thermoelastic stress range,  $S$ . This involves conversion of the fictitious elastic cycle into the actual elastoplastic-creep cycle based on assumptions for the growth of plastic and creep strains. The conversion of elastic strain into plastic strain will be performed by two different approaches in Sections 3.2.4-3.2.5. The conversion of elastic strain into creep strain during the creep dwell is described first.

### 3.2.3 Strain accumulated during a creep dwell

Consider the situation where a volume of material local to the stress concentration creeps during the high temperature dwell period, but is surrounded by material at a much lower stress that effectively only deforms elastically during the dwell. The creep strain generated during the dwell period is accommodated by the change of elastic deformation of the creeping volume and the surrounding elastic region. This results in relaxation of the stress locally. The combined effect of elastic deformation of the local and surrounding material on the stress relaxation can be expressed in terms of an elastic follow-up factor,  $Z$  [20], determined by the following uniaxial idealisation. By assuming that the elastic volume with an effective stiffness,  $E_{ef}$ , is connected in series with the creeping location, i.e. stress is common, the conversion of elastic strain into creep strain for a uniaxial stress state occurs according to:

$$\frac{\dot{\sigma}}{E} + \dot{\epsilon}_o \left( \frac{|\sigma|}{\sigma_o} \right)^n \text{sgn}(\sigma) \exp(x) = -\frac{\dot{\sigma}}{E_{ef}} \rightarrow Z \frac{\dot{\sigma}}{E} + \dot{\epsilon}_o \left( \frac{|\sigma|}{\sigma_o} \right)^n \text{sgn}(\sigma) \exp(x) = 0 \quad (9)$$

where  $Z = (E + E_{ef})/E_{ef}$ . We can distinguish two extremes: stress relaxation under constant total local strain when  $E_{ef} \rightarrow \infty$  and  $Z = 1$ , and relaxation under constant stress when  $E_{ef} \rightarrow 0$  and  $Z \rightarrow \infty$ . Based on the known compressive stress at the beginning of the creep dwell,  $\sigma_2$  (point 2 in Fig 4a), we can integrate Eq (9) over the dwell period,  $t_{dwell}$ , to deduce the stress at the end of the dwell,  $\sigma_3$  (point 3 in Fig 4a) and the creep strain accumulation,  $\epsilon_{cr}$ , via:

$$\sigma_3 = \frac{\sigma_2}{\left[ 1 + (n-1) \frac{E}{Z} \frac{\dot{\epsilon}_o}{\sigma_o^n} t_{dwell} |\sigma_2|^{n-1} \exp(x) \right]^{\frac{1}{n-1}}} \quad (i)$$

$$\epsilon_{cr} = \frac{(\sigma_2 - \sigma_3)}{(E/Z)} \quad (ii)$$
(10)

where note that  $\epsilon_{cr} > 0$  if  $\sigma_2 > 0$  and that  $\epsilon_{cr} < 0$  if  $\sigma_2 < 0$ , so that during the dwell of Fig 4a the creep strain accumulated is compressive. We will use Eq (10) to calibrate  $Z$  for the critical location of all the configurations in Figs 1c-e, based on FE simulations.

### 3.2.4 Calculation of strain range $\Delta\varepsilon$ over the cycle- constant strain approach

Fatigue life predictions are generally based on models which express the number of cycles to failure in terms of the total strain range [35], so the important feature of the cyclic response of Fig 4a is the total strain range  $\Delta\varepsilon$ . The simplest calculation of  $\Delta\varepsilon$  assumes that the total strain in the absence of plasticity (fictitious elastic state) remains the same in the presence of plasticity (constant strain approach) on the basis that thermal loading can potentially impose strong kinematic determinacy. This is inconsistent with Fig 4a, as it implies that the end of first heat-up i.e. point 2, instead occurs at point 2', and that  $\varepsilon_{p_{cooldown}}$  occurs between points 4 and 5' instead of 4 and 5 etc. According to this overly non-conservative approach the total strain range remains  $\Delta\varepsilon = S/E$ . However, this is valid only for  $Z = 1$  where point 3 in Fig 4a would lie in the same vertical axis as point 2, in which case the constant strain approach implies that  $\Delta\varepsilon = S/E$  is equal to the sum of any combination of the magnitudes of  $\varepsilon_{cr}$ ,  $\varepsilon_{p_{heatup}}$  and  $\sigma_3/E$ . For the general case  $Z > 1$  this is not true and a calculation of  $\varepsilon_{cr}$  via Eq (10(ii)) is necessary to determine  $\Delta\varepsilon$  by:

$$\Delta\varepsilon = \varepsilon_{p_{heatup}} + |\varepsilon_{cr}| + (|\sigma_3| + \sigma_{y_0})/E \quad (11)$$

in which for regime II i.e.  $\sigma_{y_0} < S \leq \sigma_{y_0} + \sigma_{y_{Tmax}}$  we use  $\varepsilon_{p_{heatup}} = 0$  and compute  $\sigma_3$  from Eq (10(i)) for  $\sigma_2 = \sigma_{y_0} - S$ , whereas for regime III i.e. when  $S > \sigma_{y_0} + \sigma_{y_{Tmax}}$  we use  $\varepsilon_{p_{heatup}} = (S - \sigma_{y_0} - \sigma_{y_{Tmax}})/E$  and  $\sigma_2 = -\sigma_{y_{Tmax}}$  in Eq (10(i)) to find  $\sigma_3$ .

### 3.2.5 Calculation of strain range $\Delta\varepsilon$ over the cycle - constant energy approach

Our more elaborate and more conservative calculation assumes that the total strain in the critical hole location increases with plasticity such that an energy density quantity instead remains the same between the fictitious elastic and elastoplastic states (constant energy approach), on the basis that the transition between these two states imposes a redistribution of the stress and strain fields [34]. The original rule by Neuber [23] considers that the sum of the fictitious elastic strain and complementary strain energy density,  $E_{e_{Neuber}} = S^2/E$ , is preserved (elastic rectangular areas between pink dashed lines in Fig 4a), whereas the Molski-Glinka [24] scheme states that this is true only for the strain energy density,  $E_{e_{Molski-Glinka}} = S^2/2E$  (elastic triangular areas in Fig 4a), leading to the following relations for the first absolute elastoplastic strain change,  $\varepsilon_{ep_{02}}$  (loading from no previous stress-strain history) and the elastic-perfectly plastic material considered here under a uniaxial stress state:

$$\begin{aligned} \frac{S^2}{E} &= \sigma_{y_{Tmax}} \varepsilon_{ep_{02}} & (i) \quad & \text{Neuber} \\ \frac{S^2}{2E} &= \sigma_{y_{Tmax}} \varepsilon_{ep_{02}} - \frac{\sigma_{y_{Tmax}}^2}{2E} & (ii) \quad & \text{Molski - Glinka} \end{aligned} \quad (12)$$

For cyclic loading, energies are calculated from the point of loading/unloading, such that for a subsequent heat-up we replace  $\sigma_{y_{Tmax}}$  with  $\sigma_{y_0} + \sigma_{y_{Tmax}}$  in Eqs (12) and calculate the absolute elastoplastic strain change,  $\varepsilon_{ep_{52}}$  (point 5 to point 2 – see Fig 4a) to determine the total strain range,  $\Delta\varepsilon$  (for a uniaxial stress state) based on the strains associated with the heat-up as:

$$\Delta\varepsilon = \frac{S^2}{E(\sigma_{y_0} + \sigma_{y_{T_{max}}})} + |\varepsilon_{cr}| + |\varepsilon_{e_{23}}| \quad (i) \quad \text{Neuber}$$

(13)

$$\Delta\varepsilon = \frac{S^2 + (\sigma_{y_0} + \sigma_{y_{T_{max}}})^2}{2E(\sigma_{y_0} + \sigma_{y_{T_{max}}})} + |\varepsilon_{cr}| + |\varepsilon_{e_{23}}| \quad (ii) \quad \text{Molski – Glinka}$$

where the first term is equivalent to  $\varepsilon_{ep_{52}}$  (see Fig 4a), the creep dwell strain,  $\varepsilon_{cr}$ , is computed from Eqs (10) and the absolute elastic strain reduction  $\varepsilon_{e_{23}}$  is defined in Section 3.2.2. Equivalently,  $\Delta\varepsilon$  can also be obtained based on the strain associated with the cool-down, which solely involves the calculation of the absolute elastoplastic strain change,  $\varepsilon_{ep_{35}}$ , by:

$$\Delta\varepsilon = \varepsilon_{ep_{35}} = \frac{S^2}{E(\sigma_{y_0} + |\sigma_3|)} \quad (i) \quad \text{Neuber}$$

(14)

$$\Delta\varepsilon = \varepsilon_{ep_{35}} = \frac{S^2 + (\sigma_{y_0} + |\sigma_3|)^2}{2E(\sigma_{y_0} + |\sigma_3|)} \quad (ii) \quad \text{Molski – Glinka}$$

It is useful to recognise that the calculations of  $\varepsilon_{ep_{52}}$  and  $\varepsilon_{ep_{35}}$  are solely based on the allowable elastoplastic stress range and are independent of each other. Therefore, the condition,  $\varepsilon_{cr} + \varepsilon_{p_{heatup}} = \varepsilon_{p_{cooldown}}$ , will not be generally satisfied, i.e. a closed inelastic cycle is not predicted. This implies the following two possible scenarios for the cyclic predictions of the constant energy approach:

1. Since  $\varepsilon_{ep_{52}}$  is calculated based on a stress range,  $\sigma_{y_0} + \sigma_{y_{T_{max}}}$ , larger than the range,  $\sigma_{y_0} + |\sigma_3|$ , associated with  $\varepsilon_{ep_{35}}$ , for each subsequent heat-up calculation via Eqs (13) the method can give  $|\varepsilon_{cr} + \varepsilon_{p_{heatup}}| < |\varepsilon_{p_{cooldown}}|$ . This will produce an unphysical drift towards tensile strains i.e. the second heat-up will be predicted to occur at a point 7 (see Fig 4a).
2. Since the calculation of  $\varepsilon_{ep_{35}}$  does not take into account that at the initial state,  $\sigma_3$ , (point 3), creep strain has accumulated under an elastic follow-up factor,  $Z > 1$  (in the general case), for each subsequent heat-up calculation the method can also give  $|\varepsilon_{cr} + \varepsilon_{p_{heatup}}| > |\varepsilon_{p_{cooldown}}|$ . This will cause an unphysical drift towards compressive strains.

The above imply that Eqs (13-14) generally lead to different predictions of  $\Delta\varepsilon$ , and whether the condition 1 or 2 prevails will depend on the creep dwell characteristics. We can introduce some sort of dependency between the  $\varepsilon_{ep_{52}}$  and  $\varepsilon_{ep_{35}}$  calculations. For example, we can add to Eqs (14) the additional creep strain,  $\varepsilon_{cr_z} = (Z - 1)(\sigma_2 - \sigma_3)/E$ , that occurs for  $Z > 1$  with respect to the case,  $Z = 1$ . The merits of this correction and the suitability of Eqs (13-14) in predicting  $\Delta\varepsilon$  will be demonstrated through our results later in Section 4.4.

It is also useful to recognise that the current calculation scheme will generally overpredict plastic strain, due to the assumption surrounding Fig 4a (Section 3.2.2), in that the temperature dependence of the yield stress,  $\sigma_{y_T}$ , is not taken into account plastic strain is assumed to accumulate at the extremes of the cycle, i.e. when the yield stress equals  $\sigma_{y_{T_{max}}}$  or  $\sigma_{y_0}$ . In fact, depending on the rate



that the outer surface temperature and thermal difference across the hot layer are increased, as well as the material's constitutive dependence of  $\sigma_{y_T}$  upon temperature, plastic deformation and therefore energy dissipation can occur during heat-up and cool-down when  $\sigma_{y_T} > \sigma_{y_{T_{max}}}$ . The importance of this effect is explored by an incremental implementation of the constant energy approach, which also allows for creep strain growth during heat-up and cool-down to be taken into account in an explicit (Euler) manner. In Fig 5 we present our pseudo-analytical algorithm for a time increment,  $dt$ , during a subsequent heat-up, i.e. between points 6 and 2 in Fig 4a; note that here we use absolute stress values.

The term  $dS$  is the fictitious elastic stress increment based on the known thermal gradient increment  $d\Delta T$ ;  $dE_{e_{Neuber}}$  and  $dE_{e_{Molski-Glinka}}$  are the elastic energy increments based on Neuber and Molski-Glinka rules, and  $dE_{ep_{Neuber}}$ ,  $dE_{ep_{Molski-Glinka}}$  are the corresponding elastoplastic increments;  $\sigma_t$  and  $\sigma_{t+dt}$  are the absolute stresses at the beginning and at the end of the increment;  $d\sigma$  and  $d\epsilon_{ep}$  are the stress and elastoplastic strain increments and  $d\sigma_{cr}$  is the relaxation of stress in the increment due to creep. During plastic deformation, we assume that  $Z = 1$ , whereas during the creep dwell we use the actual value of  $Z > 1$  of the elastic follow-up factor denoted in Fig 5 as  $Z_{el}$ .

1. **define**  $d\Delta T$  **with respect to**  $dt$
2.  $dS = SCF \frac{E \Delta T}{(1-\nu)} G$
3.  $S_{t+dt} = S_t + dS$
4.  $dE_{e_{Neuber}} = \frac{dS}{E} (2S_t + dS)$  **and/or**  $dE_{e_{Molski-Glinka}} = \frac{dS}{E} (S_t + \frac{dS}{2})$
5.  $\sigma_{t+dt} = \sigma_t + dS$
6. **if**  $\sigma_{t+dt} > \sigma_{y_T}$  **then**
7.      $\sigma_{t+dt} = \sigma_{y_T}$
8.      $d\sigma = \sigma_{t+dt} - \sigma_t$
9.     **if**  $d\sigma > 0$  **then**
10.          $dE_{ep_{Neuber}} = d\epsilon_{ep}(\sigma_t + d\sigma) + d\sigma \frac{\sigma_t}{E}$  **and/or**  $dE_{ep_{Molski-Glinka}} = d\epsilon_{ep}(\sigma_t + \frac{d\sigma}{2})$
11.     **else if**  $d\sigma < 0$  **then**
12.          $dE_{ep_{Neuber}} = dE_{ep_{Molski-Glinka}} = d\epsilon_{ep}(\sigma_{t+dt} + \frac{|d\sigma|}{2})$
13.     **end if**
14.     **calculate**  $d\epsilon_{ep}$  **via**  $dE_{e_{Neuber}} = dE_{ep_{Neuber}}$  **and/or**  $dE_{e_{Molski-Glinka}} = dE_{ep_{Molski-Glinka}}$
15.      $Z = 1$
16. **else**
17.      $d\epsilon_{ep} = \frac{dS}{E}$
18.      $Z = Z_{el}$
19. **end if**
20.  $\epsilon_{ep_{t+dt}} = \epsilon_{ep_t} + d\epsilon_{ep}$
21.  $d\sigma_{cr} = \dot{\epsilon}_o dt \frac{E}{Z} \left( \frac{|\sigma_t|}{\sigma_o} \right)^n \exp(x)$
22.  $\sigma_{t+dt} = \sigma_{t+dt} - d\sigma_{cr}$

Figure 5. Incremental implementation of Neuber and Molski-Glinka schemes with creep.

The condition  $d\sigma < 0$  occurs when the current yield stress is lower than the actual stress at the previous increment i.e.  $\sigma_{y_T} < \sigma_t$ , in which case the complementary energy is considered to be zero. Here we compute plasticity for  $\sigma_{y_T}$  corresponding to the temperature at the end of the increment,

while creep is calculated based on the stress at the beginning of the increment,  $\sigma_t$ . For small  $dt$  the choice of current yield stress,  $\sigma_{y_T}$ , and creep stress,  $\sigma_t$ , plays a minor role.

### 3.3 Fatigue life prediction

We now use an empirical fatigue law that predicts the cycles to fatigue crack initiation, based on the total strain range,  $\Delta\varepsilon$ , calculated in Sections 3.2.4-3.2.5, which we take as a conservative estimate of the number of cycles to failure,  $N_f$ . The Manson-Coffin law [36] predicts  $N_f$  based on the inelastic strain range,  $\Delta\varepsilon_{in}$ , in the low cycle fatigue (LCF) regime whereas Basquin's law [37] predicts  $N_f$  based on the elastic range,  $\Delta\varepsilon_e$ , in the high cycle fatigue (HCF) regime. Fatigue experiments are typically performed under total strain,  $\Delta\varepsilon$ , controlled conditions and therefore CMSX-4 fatigue parameters that are available in the literature are calibrated for a combined Basquin and Manson-Coffin law which relates  $\Delta\varepsilon$  with  $N_f$ . Here we use one such law that has also been extended by Scholz et al [35] to account for temperature dependence as follows:

$$\Delta\varepsilon = A_1[\tau(C + \log N_f)]^{B_1} + A_2[\tau(C + \log N_f)]^{B_2} \quad (15)$$

where  $A_1 = 202$ ,  $B_1 = -2.58$ ,  $A_2 = 0.199$ ,  $B_2 = -0.04$ ,  $C = 3.01$ , are CMSX-4 constants fitted to uniaxial fatigue experiments under constant  $\Delta\varepsilon$ , along the  $\langle 001 \rangle$  orientation [35], in the temperature range, 850 – 1050 °C. Although Scholz et al introduced  $\tau = (T + 273)/10^3$  to account for the reduction of  $N_f$  with temperature,  $T$ , here our cycle involves equal amounts of inelastic strain during cooldown and during heat-up (Section 3.2.2). As fatigue data at room temperature for the required conditions are not available, we define  $\tau$  based on  $T = 850$  °C and assume a temperature independent fatigue curve; for known  $\Delta\varepsilon$ ,  $N_f$  is calculated numerically via Eq (15).

## 4 Results

### 4.1 FE thermoelastic results

We first present results from elastic FE analysis in Fig 6, in order to provide the essential value of the SCF at the critical film hole location and to validate our theoretical analysis in Section 3.1. We use maximum absolute principal stress contours,  $\sigma = \max(|\sigma_{max}|, |\sigma_{med}|, |\sigma_{min}|)$ , normalised by  $Ea\Delta T$  in Fig 6a and by  $Ea\Delta T/(1 - \nu)$  in Figs 6b-d. In both Figs 6a-b, the cool layer undergoes pure tension while the hot layer is subjected to combined bending and compression, in agreement with Eqs (3). 2D plane stress double flat layers in which  $\varphi_\theta$  rotations are not allowed to occur (Fig 6a), result in a similar stress field to 3D long cylindrical layers that satisfy  $R \gg b_1$ ,  $R \gg L$  and  $R \gg H$  (Fig 6b), if the scaling factor  $1/(1 - \nu)$  is applied. This justifies the use of the flat 2D plane stress and axisymmetric models in Fig 1c for studying inelastic phenomena in the absence of holes.

In the presence of holes (Figs 6c-d) the above stress field characteristics continue to apply, whilst local stress concentration effects are superimposed. The film hole inclination,  $\gamma = 60^\circ$  (Fig 6c) results in a very large maximum stress concentration of  $SCF = 3.85$ , whereas the transverse film hole (Fig 6d) only gives  $SCF = 1.85$ . The larger SCF for  $\gamma = 60^\circ$  is due to the fact that the critical location lies in the vicinity of an acute wedge, of angle  $90^\circ - \gamma$ , which also coincides with an elliptical vertex generated by the intersection of the circular hole profile with the plane of the layer [14]; the ellipticity of the outer (and inner) rim of the film hole can be described in terms of the ratio of major to minor diameters,  $D_{OM}/D_{Om} = 1/\cos\gamma$ . The stress state at the location of the max SCF for  $\gamma = 0^\circ$  (Fig 6d) is uniaxial ( $\sigma_{max} = \sigma_{med} = 0$ ), whereas for  $\gamma = 60^\circ$  the state is weakly biaxial, with a ratio of minimum principal to medium principal stress,  $\sigma_{min}/\sigma_{med} \approx 6$  ( $\sigma_{max} = 0$ ). Therefore, the  $SCF =$

3.85 is defined here by dividing the equivalent stress,  $\sigma_{eq} = \sqrt{\sigma_{med}^2 - \sigma_{med}\sigma_{min} + \sigma_{min}^2}$ , over the corresponding nominal equibiaxial stress in the absence of the hole.

## 4.2 FE inelastic results

We now provide FE results in Fig 7 which reveal the actual effects of the hole stress concentration in the inelastic regime, by applying the thermal cycle defined in Section 2.2 and illustrated in Fig 2. For computational efficiency, we have modelled the systems in Figs 6c-d inelastically through the equivalent models (Figs 1d-e) in which the max SCF at the critical film hole location is the same, e.g. the exact value of max SCF = 3.85 at the acute wedge of the film hole in Fig 6c is generated in Fig 1e by adjusting the length/width of the plates; in the same manner, the pedestal spacing,  $L$ , in Fig 1d is adjusted to give the max SCF = 1.85 that is observed in Fig 6d. For the axisymmetric-transverse hole model (Figs 7a – a'') we apply 100 cycles, whereas for the full 3D inclined hole model (Figs

### thermoelastic FE results

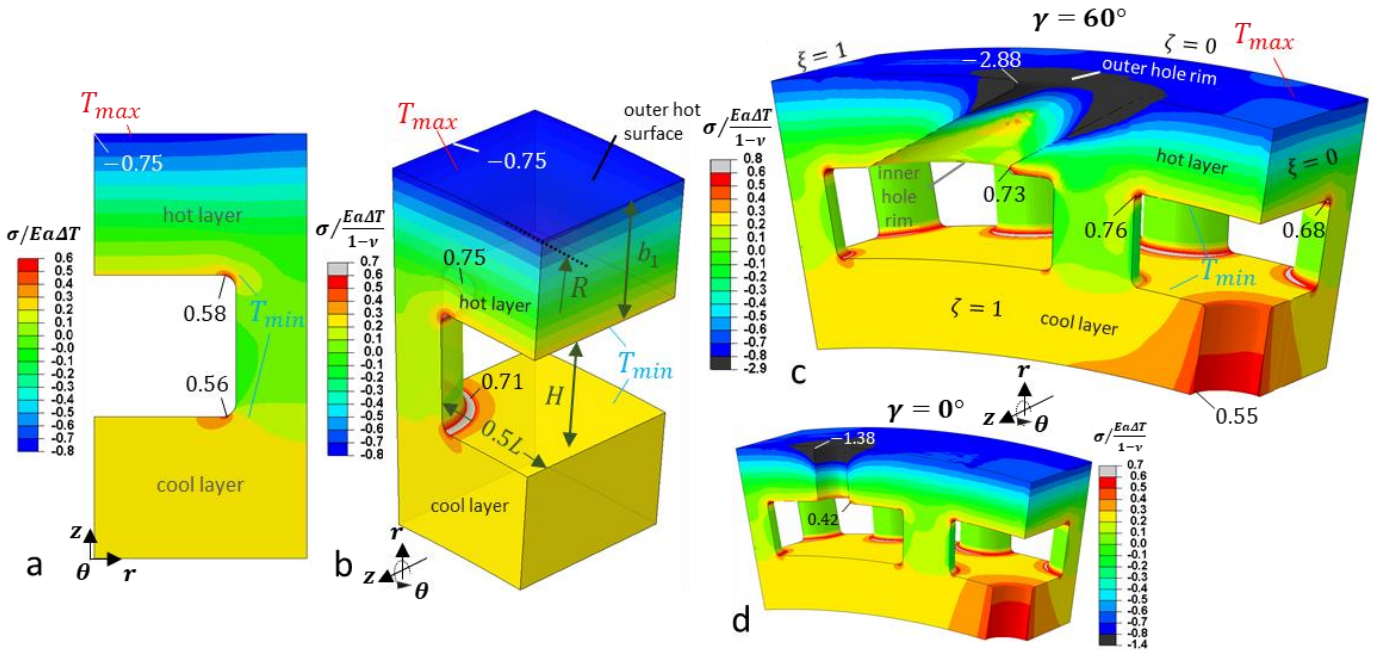


Figure 6. FE stress results from thermoelastic analysis. (a) 2D plane stress model. (b) Cylindrical double layer model with no holes, obtained by using a 1/3 of the model in Fig 5(c). (c) Cylindrical model with inclined film hole. (d) Cylindrical model with transverse hole. The contours represent maximum absolute principal stress.

7b – b'' and 7c – c'') we apply 30 cycles due to the significant computational cost involved. The  $\varepsilon_{peq_{cool-down}}$  contours in Figs 7a'', b'', c'' are obtained by dividing the equivalent plastic strain accumulated over all the cool-down periods by the total number of cycles; in the same manner,  $\varepsilon_{creq}$  in Figs 7a', b', c' is calculated as the equivalent creep strain accumulation per cycle as an average throughout the cyclic history. We use accumulated strain quantities here to immediately verify that the location experiencing the largest amount of inelastic strain coincides with the location of max SCF in the elastic simulations of Fig 6(c-d).

The characteristic instances 1-7 of the hypothetical cycle, outlined earlier in Section 3.2.2 and denoted in Fig 4a, are indicated here for the first and second cycle (1-2) in Fig 7b. For the nearly uniaxial stress state of  $\gamma = 60^\circ$  (Figs 7b-c) we plot minimum principal strain,  $\varepsilon_{min}$ , versus minimum principal stress,  $\sigma_{min}$ , whereas for the uniaxial case of  $\gamma = 0^\circ$  (Fig 7a) we plot the circumferential,

$\theta$ , stress-strains. For  $\gamma = 60^\circ$  (Figs 7b-c) the direction of  $\sigma_{min}-\epsilon_{min}$ , is approximately constant through the cycle and approximately coincides with the  $y$  axis (see Fig 7b'). A major difference between the hypothetical cycle of Fig 7a and the actual cycle in Fig 7b is that after the onset of yield (point 1) the stress initially increases due to the slight increase of yield stress,  $\sigma_{y_T}$ , with temperature,  $T$  (Fig 3a), and then the decrease of  $\sigma_{y_T}$  at higher  $T$  dominates, such that the stress decreases drastically down to point 2, where the creep dwell begins. For  $\gamma = 60^\circ$  this effect is less pronounced at  $\Delta T = 150^\circ\text{C}$  (Fig 7c), as the inelastic strain through the cycle is much smaller compared to the case  $\Delta T = 400^\circ\text{C}$ , which is associated with extreme strains (Fig 7b). This is consistent with Fig 7c'', which shows that plasticity for  $\Delta T = 150^\circ\text{C}$  is largely localised in the vicinity of the acute wedge, as opposed to Fig 7b'' where it occupies a much larger volume. Severe plasticity effects also occur for  $\gamma = 0^\circ$  in Figs 7a – a' but this is the consequence of a significantly higher thermal difference,  $\Delta T = 600^\circ\text{C}$ , and despite this, the inelastic strain range through the cycle of Fig 7a is still much smaller than the corresponding range in Fig 7b.

A common effect in Figs 7a-b is that although the cycle saturates in terms of stress instantly, i.e. within cycle 1-2, this does not occur in terms of strain, for which a drift towards tensile values is evidenced with subsequent cycling due to the tensile plastic strain growth on cooldown being higher than the sum of creep and plastic strains at high temperature. To interpret this effect we first assume that for regions where reverse plasticity does not occur, i.e. surrounding the critical location, a large number of cycles may be necessary for the stress through the cycle to reach a cyclic state [29]. As a result, the increase of the creep strain in these regions can occur over a large number of cycles, during which the plastic strain field generated on cooldown must continuously change to satisfy compatibility. This implies that our results in Figs 7a-c do not strictly correspond to the cyclic stress-strain state [29]. However, for the critical film hole location, where severe plasticity occurs, we have noted that the effect of the above phenomenon on the inelastic strain history results is small and only slightly increases the rate at which the inelastic strain drifts within the first 10-20 cycles. After this transient response, the inelastic drift rate towards tensile strains is approximately constant, indicating that other mechanisms operate; for example, the inelastic strains in Fig 6c initially drift towards compressive states i.e. cycle 10, after which the effect of the extra tensile plastic strain on each cooldown eventually prevails, moving the response back towards tensile states (cycle 30 virtually coincides with the initial cycle 1-2).

The driving mechanism can be characterised as local ratcheting at the critical film hole location and may be related to the fact that reverse plasticity occurs in regions adjacent to a free surface. As this mechanism can also be sensitive to the constitutive plasticity law (note here we have assumed perfect plasticity) [38], we give priority here to focusing on the constant cyclic strain range,  $\Delta\epsilon$ , that gives rise to low cycle fatigue. Discussion on the mechanism is provided later in Section 5.

### 4.3 Cyclic predictions using a local strain approach

Before presenting fatigue life results, we first demonstrate in Fig 8 the accuracy with which the incremental Neuber, Molski-Glinka and constant strain local approaches predict the inelastic cycle. The different elastic-follow up factors,  $Z$ , that we calibrate based on the FE results and use in the local strain approach for the cases of Figs 8a-d (for the creep dwell) are presented in Table 1. The table specifically shows how the value of  $Z$  changes between the first creep dwell and the second creep dwell. This will be discussed in the following paragraphs – for now, the results of the local approaches in Fig 8 are based on the large values of  $Z$ , i.e. for the first creep dwell.

A main feature in Fig 8 is that when thermal loading is severe, i.e.  $\Delta T = 600^\circ\text{C}$  for a transverse hole,  $\gamma = 0^\circ$  (Fig 8a) and  $\Delta T = 400^\circ\text{C}$  for an inclined hole,  $\gamma = 60^\circ$  (Fig 8c), the Neuber approach is overly conservative. The opposite is shown for the constant strain approach, in agreement with the

# inelastic FE results

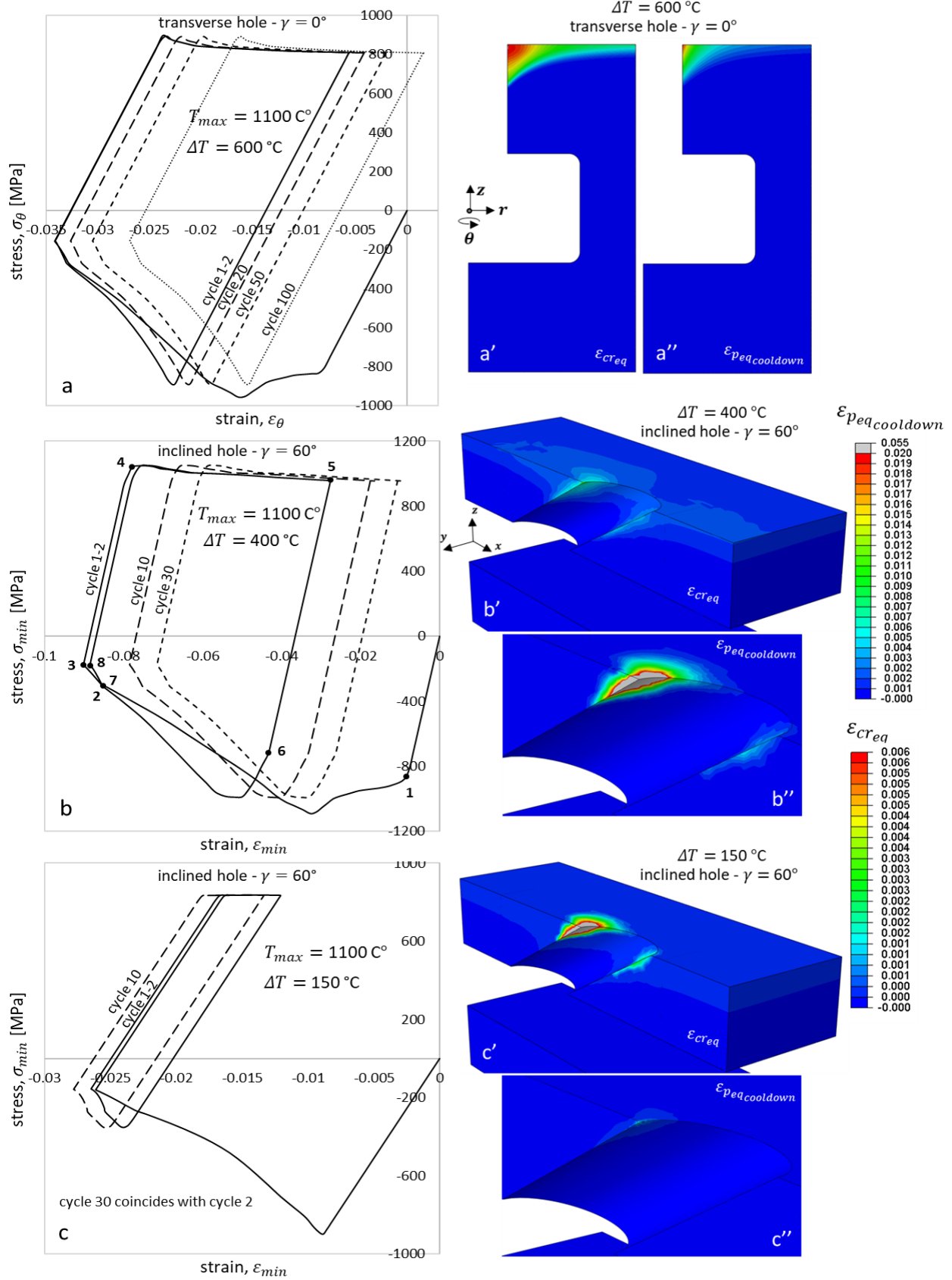


Figure 7. FE results from inelastic cyclic analysis for  $T_{max} = 1100\text{ }^{\circ}\text{C}$ . (a) Inelastic stress-strain cycle for transverse hole -  $\gamma = 0^{\circ}$  for  $\Delta T = 600\text{ }^{\circ}\text{C}$ . (a') Creep strain accumulation per cycle for  $\gamma = 0^{\circ}$ . (a'') Plastic strain accumulation on cool-down, per cycle, for  $\gamma = 0^{\circ}$ . In the same order (b-b'') show the results for the inclined hole -  $\gamma = 60^{\circ}$  for  $\Delta T = 400\text{ }^{\circ}\text{C}$ . The corresponding results for  $\Delta T = 150\text{ }^{\circ}\text{C}$  (and  $\gamma = 60^{\circ}$ ) are shown in (c-c').

literature [34, 39]. The Molski-Glinka scheme is deemed superior for predicting the total strain range,  $\Delta\varepsilon$ , both at high  $\Delta T$  (Figs 8a,c) and low  $\Delta T$  (Figs 8b,d). The overprediction of plastic strain by the Neuber approach can be related to the fact that Figs 8a,c correspond to the cases shown earlier in Figs 7a'',b'', where plasticity is not confined to the location of the stress concentration. Evidently, in Figs 8b,d where we reduce  $\Delta T$  such that plasticity is more localised at the critical hole location (shown earlier in Fig 7c'' for  $\gamma = 60^\circ$ ), the agreement of all three local strain approaches with the FE cycle is greatly improved. In general, the constant strain approach provides more accurate predictions for  $\gamma = 0^\circ$  (Figs 8c-d) than for  $\gamma = 60^\circ$  (Figs 8c-d), implying that the transverse hole where the stress concentration factor is  $SCF = 1.85$  imposes stronger kinematic determinacy at the critical location than the inclined hole where  $SCF = 3.85$ .

We acknowledge that in Fig 8c the local strain approaches and FE analysis predict different stresses at cooldown. On the basis of the low biaxiality ratio,  $\sigma_{min}/\sigma_{med} \approx 6$ , seen in the elastic FE simulations for  $\gamma = 60^\circ$  (Section 4.1), our local strain calculations have adopted the common assumption [40] that a weakly biaxial state is preserved in the inelastic regime and therefore consider a single stress-strain component. In fact, the inelastic biaxial stress ratio is found to increase to  $\sigma_{min}/\sigma_{med} \approx 3$ , which explains why the minimum principal stress,  $\sigma_{min}$ , exceeds the von Mises yield stress at room temperature,  $\sigma_{y_0} = 805$  MPa, on cooldown in Fig 8c. However, the difference between the strain range in terms of  $\varepsilon_{min}$  and in terms of the equivalent strain,  $\varepsilon_{eq}$ , is found to be significantly lower (not shown). In addition, when  $\Delta T = 150$  °C (which is a more realistic thermal loading scenario for this application), Fig 8d shows that the disagreement between  $\sigma_{min}$  and  $\sigma_{y_0}$  vanishes. As a result, extending our local strain calculations to account for multiaxial states is not considered to add significant value here, in the sense that holes generally impose a very strong degree of uniaxiality at the free surface. Also note that a particular inclined hole  $\gamma = 60^\circ$  is studied here as an extreme case. In practise, film holes are manufactured with diffuser type shapes and/or at lower inclinations,  $\gamma$ , which are both expected to reduce drastically the acute wedge angle at the outer hole rim (that is responsible for the non-zero  $\sigma_{med}$  component here) in combination with the absence of a hole fillet.

To identify the merits of the incremental implementation of the local strain approaches, we have also predicted the cycles in Fig 8 in a non-incremental manner i.e. by applying Eqs (12) to determine the first elastoplastic strain,  $\varepsilon_{ep_{02}}$  (first heat-up), followed by Eqs (10) to calculate the creep strain,  $\varepsilon_{cr}$ , (first creep dwell between points 2-3); thereafter Eqs (14) is used to determine the elastoplastic strain,  $\varepsilon_{ep_{35}}$ , on first cooldown and finally Eqs (13) to determine  $\varepsilon_{ep_{52}}$  on subsequent heat-up. We will not illustrate the non-incremental cycle predictions, but instead discuss the important features. Since this simpler non-incremental method does not account for intermediate yield stress values during heat-up, for the first heat-up it predicts a plastic plateau response similar to the idealised cycle shown earlier in Fig 4a. Therefore, the additional energy dissipation during first heat-up is ignored and the first elastoplastic strain,  $\varepsilon_{ep_{02}}$ , is largely overestimated, such that the cycle is predicted to occur at unrealistic compressive mean strains (not shown). However, the error due to not taking into account the intermediate yield stresses was generally found to be much less significant in the calculation of strain for subsequent heat-ups  $\varepsilon_{ep_{52}}$  (not shown), both at high and low  $\Delta T$  values. With regards to the calculation of strain on cooldown, the non-incremental calculation of  $\varepsilon_{ep_{35}}$  is generally found to be approximately the same as the result of the incremental calculation, suggesting that the incremental implementation is not necessary here since the strain range,  $\Delta\varepsilon$ , is only considered for fatigue life predictions. If the mean strain range is important and/or if transient temperature effects



in the structure cause a more complex local thermoelastic stress history [18] and/or if more elaborate material constitutive laws are used, then the incremental method is essential.

As denoted in Figs 8b,d and discussed in Section 3.2.5, a feature from which both the incremental and non-incremental local strain approaches suffer, is that a closed inelastic cycle cannot be predicted i.e. point 7 (end of subsequent heat-up) does not coincide with point 2 (end-of first subsequent heat-up) and as a result point 8 (end of subsequent creep dwell) does not coincide with point 3 (end of first creep dwell). Therefore, for consistency with Fig 8 in our discussion here we will refer to the calculation of  $\varepsilon_{ep_{52}}$  according to Eq (13) by the term  $\varepsilon_{ep_{57}}$ . Based on Neuber's rule our cycle in most cases drifts towards tensile strains (Figs 8a-c), indicating that the absolute elastoplastic strain on heat-up,  $\varepsilon_{ep_{57}}$  (see points in Fig 8d) is underpredicted. Instead, the Molski-Glinka and constant strain approaches predict a drift towards the opposite direction (Figs 8a-d) i.e. the cooldown strain,  $\varepsilon_{ep_{35}}$ ,

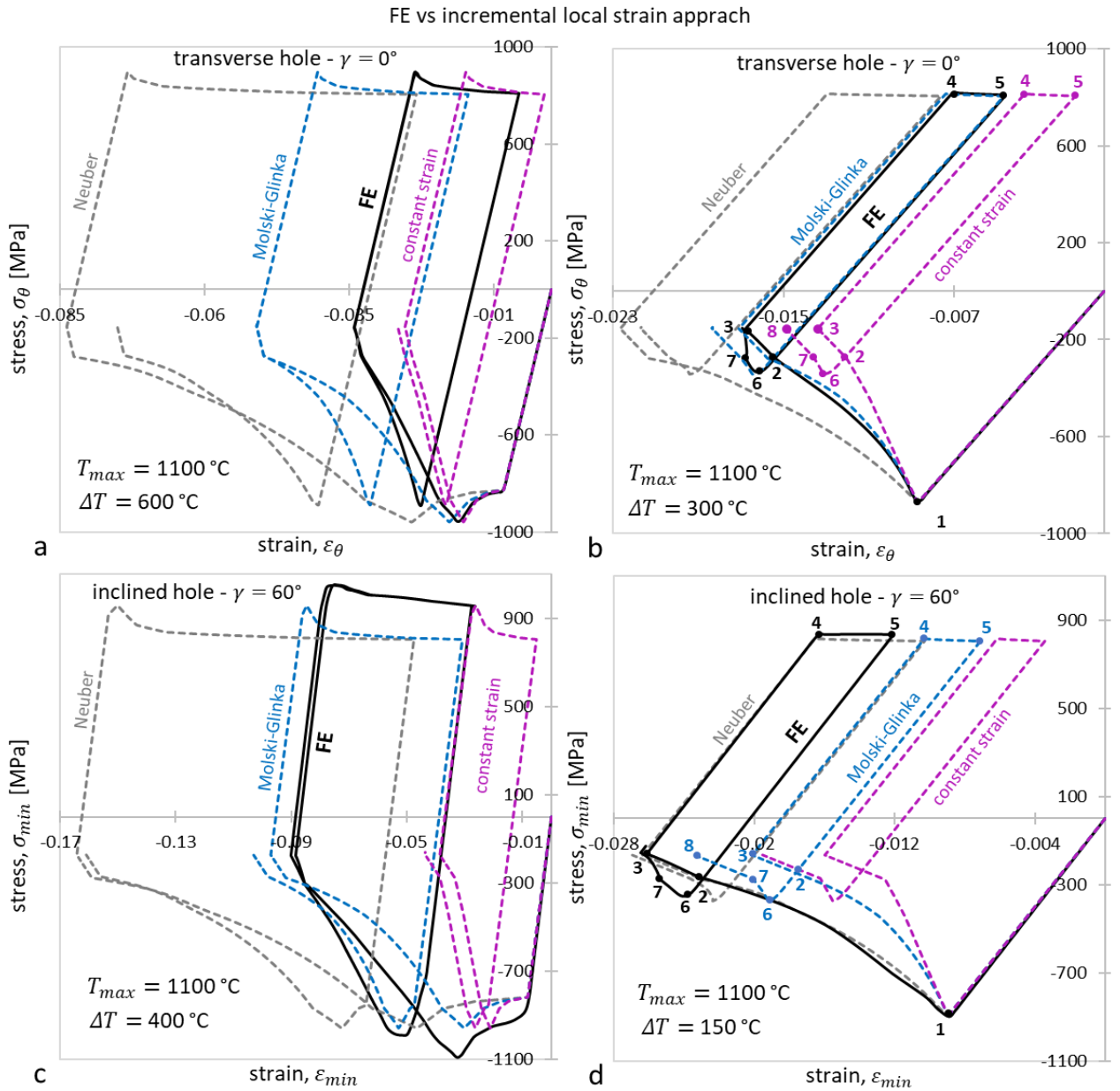


Figure 8. Agreement between FE cyclic results and the results of the incremental local strain scheme based on Neuber, Molski-Glinka and constant strain approaches, for  $T_{max} = 1100^\circ\text{C}$ . (a) Case of transverse hole -  $\gamma = 0^\circ$  for  $\Delta T = 600^\circ\text{C}$ . (b) Case of  $\gamma = 0^\circ$  for  $\Delta T = 300^\circ\text{C}$ . (c) Case of inclined hole -  $\gamma = 60^\circ$  for  $\Delta T = 400^\circ\text{C}$ . (d) When  $\gamma = 60^\circ$  for  $\Delta T = 150^\circ\text{C}$ .



is underpredicted. An observation related to our argument that the underprediction of  $\varepsilon_{ep_{35}}$  is caused by the inability of the cooldown strain calculation to account for the additional creep dwell strain,  $\varepsilon_{cr_z}$ , between the actual case,  $Z > 1$  and the case,  $Z = 1$ , can be made for Fig 8d. In this figure, the contribution of creep dwell strain (inelastic strain between points 2-3 or points 7-8 in the Molski-Glinka cycle of Fig 8d) to the inelastic strain of the cycle is the maximum amongst all the cases shown in Figs 8a-d, and this is the only case where the implementation of Neuber predicts that the cycle drifts toward compressive strains.

As discussed in Section 3.2.5, we can predict a larger and potentially more accurate  $\varepsilon_{ep_{35}}$  value by including the creep strain,  $\varepsilon_{cr_z}$ , in the cooldown calculation (Eqs (14)). Indeed, we find that for most scenarios in Fig 8, this correction eliminates the drift towards compressive strains, predicting almost closed cycles (not shown). A feature of the FE solution that can be related to the dependence between the creep dwell strain and the plastic strain on cooldown in Fig 8b, is the following. After the first cooldown, there is an additional plastic strain on subsequent heat up (between points 6-7 in the FE cycles of Figs 8b,d) and therefore the creep strain on the second creep dwell (points 7-3 in FE cycles of Figs 8b,d) is much smaller than during the first creep dwell (points 2-3 in FE cycles of Figs 8b,d). As a result, the first dwell in the FE cycle of Fig 8d occurs when  $Z \approx 4.2$ , whereas the second when  $Z \approx 2$ ; the same occurs in Fig 8b ( $Z$  changes from 2.2 to 1.2) as well as in many cases included in Table 1. We can specifically see in Table 1 that the significant changes of  $Z$  occur at low  $\Delta T$  values, where plasticity becomes less dominant. From a theoretical point of view, these phenomena highlight that non-local effects are at play, which cannot be physically captured by the local strain approaches. From a practical point of view, this phenomenon indicates that when the total strain range,  $\Delta\varepsilon$ , is calculated based on the strain on a subsequent heat-up i.e. Eqs (13), the value of  $Z$  during the second creep dwell should be used from Table 1.

Table 1. Elastic follow-up factors during the first and the second creep dwell.

$T_{max}$ (°C)	$\Delta T$ (°C)	elastic follow-up factors $Z$				
		2D plane stress/axisymmetric flat layers (Fig 1c) $b_2/b_1 = 1$	3D axisymmetric flat layers with transverse hole $\gamma = 0^\circ$ (Fig 1d) $b_2/b_1 = 1$	3D model with inclined hole $\gamma = 60^\circ$ (Fig 1e) $b_2/b_1 = 0.2$	3D model with inclined hole $\gamma = 60^\circ$ (Fig 1e) $b_2/b_1 = 1$	3D model with inclined hole $\gamma = 60^\circ$ (Fig 1e) $b_2/b_1 = 1.5$
1100	880	1.15 → 1.15	1.9 → 1.8	-	-	-
	600	-	2 → 1.8	5.4 → 4.8	3 → 2.5	4 → 4
	400	-	2.2 → 1.8	5.1 → 3	6 → 3	3.5 → 3.4
	300	-	2.2 → 1.2	5.1 → 2.2	5.5 → 2.5	2.8 → 2.5
	220	-	-	4.8 → 2	5 → 2.3	3.8 → 2
	150	-	-	5.1 → 2	4.2 → 2	3.9 → 2
used for fatigue (Figs 8-9)			1.6	2.05	2.45	2.45
900	880	1.15 → 1.15	1.15 → 1.15	-	-	-
	600	-	1.35 → 1.15	-	2.9 → 2.7	-
	400	-	1.4 → 1.1	-	2.2 → 2.1	-
	300	-	-	-	2.2 → 1.8	-
	220	-	-	-	2.9 → 2.2	-
	150	-	-	-	-	-
used for fatigue (Figs 8-9)			1.15		2	

The aim of the local strain approach, however, is to provide straightforward and reliable predictions of  $\Delta\varepsilon$ , without the need for performing inelastic cyclic FE analysis for a large number of conditions. Therefore, we will next answer the following questions:

- 1) Whether obtaining the precise value of  $Z$  for each  $\Delta T$  and  $T_{max}$  combination in Table 1 through FE simulations is necessary towards predicting fatigue life reliably,
- 2) Whether accurate life predictions can be obtained based on the cooldown strain,  $\varepsilon_{ep_{35}}$ , (Eqs (14)) which is less sensitive to  $Z$ ; note that the change of  $Z$  in Figs 8b-d does not change the stress at the end of the creep dwell,  $\sigma_3$ .

## 4.4 Fatigue life results

Fig 9 compares the FE and non-incremental local strain results in terms of cycles to failure,  $N_f$  (by using  $\Delta\varepsilon$  in Eq (15)) over a range of thermal loading,  $\Delta T$ , for the high and low levels of max temperature,  $T_{max} = 1100$  °C,  $T_{max} = 900$  °C. For each case in Fig 9, the local approach uses the value of  $Z$  for the second creep dwell in Table 1, taken as the average over the practical range of interest  $\Delta T \leq 400$  °C (values denoted in Table 1). The simplest calculation based on the thermoelastic strain,  $\Delta\varepsilon = S/E$ , (Fig 9a) has some merits for predicting fatigue at transverse holes ( $\gamma = 0^\circ$ ) for the low range  $\Delta T \leq 400$  °C of interest to the application. The advanced constant strain local approach based on Eq (11) predicts only slightly less conservative results, since the factor,  $Z$ , that causes the difference with the  $\Delta\varepsilon = S/E$  solution is small for  $\gamma = 0^\circ$  i.e.  $Z = 1.6$  and  $Z = 1.15$  (see Table 1). Both of the above two constant strain approaches lead to unrealistically high  $N_f$  values for the inclined hole ( $\gamma = 60^\circ$  - Fig 9a). For  $\gamma = 60^\circ$  only the constant energy local approaches of Neuber and Molski-Glinka provide reliable results (Fig 9b). Both of these approaches are clearly more conservative for  $\gamma = 0^\circ$  than for  $\gamma = 60^\circ$ , due to a stronger degree of kinematic determinacy for  $\gamma = 0^\circ$ . For the more critical case of  $\gamma = 60^\circ$ , in both  $T_{max} = 1100$  °C and  $T_{max} = 900$  °C, the application of Neuber (Eq 13(i)) gives a conservative prediction whereas Molski-Glinka (Eq 13(ii)) gives a non-conservative calculation, such that the FE results are bounded by these two local solutions, as reported in the literature [34].

The incremental implementation of Neuber and Molski-Glinka are found to lead to less conservative predictions here, but the effect is considered to be minor (not shown), despite the strain range,  $\Delta\varepsilon$ , in Fig 9b being determined by the strain on heat-up (and the creep dwell strain), where the non-incremental method is generally expected to introduce errors (due to the effect of the reduction of yield stress with temperature). A more interesting result here is the comparison shown in Fig 10 between the  $\Delta\varepsilon$  calculation based on heat-up and creep dwell (Fig 10a) and the calculation based on cooldown (Fig 10b) with the creep strain correction,  $\varepsilon_{cr_z}$ , for different layer thickness ratios,  $b_2/b_1$ . It is shown that fatigue life can be predicted reliably based on either of these two calculations, with the cooldown calculation (Fig 10b) giving more conservative results and a better agreement with FE. This adds credibility to the  $\varepsilon_{cr_z}$  correction and demonstrates that a non-incremental calculation of the cooldown strain for a single value of  $Z = 2.45$  (for the extreme case  $b_2/b_1 = 0.2$  we use  $Z = 2.05$ ) predicts accurately the gain in fatigue life as the cool layer thickness,  $b_2$ , is decreased. Noteworthy is that fatigue life is improved at an increasing rate with decreasing  $b_2/b_1$ , which is relevant to the boundaries of the non-linear regime plotted earlier in Fig 3b. The non-linearities arise from the fact the kinematic constraint factor,  $G$ , (Eq (5)) for the hot layer due to the presence of the cool layer increases non-linearly with  $b_2/b_1$ . This strengthens the link between our theoretical thermoelastic stress analysis (Section 3.1) and the fatigue results. The implications of our fatigue results and analysis for the transpiration cooling application are discussed next.

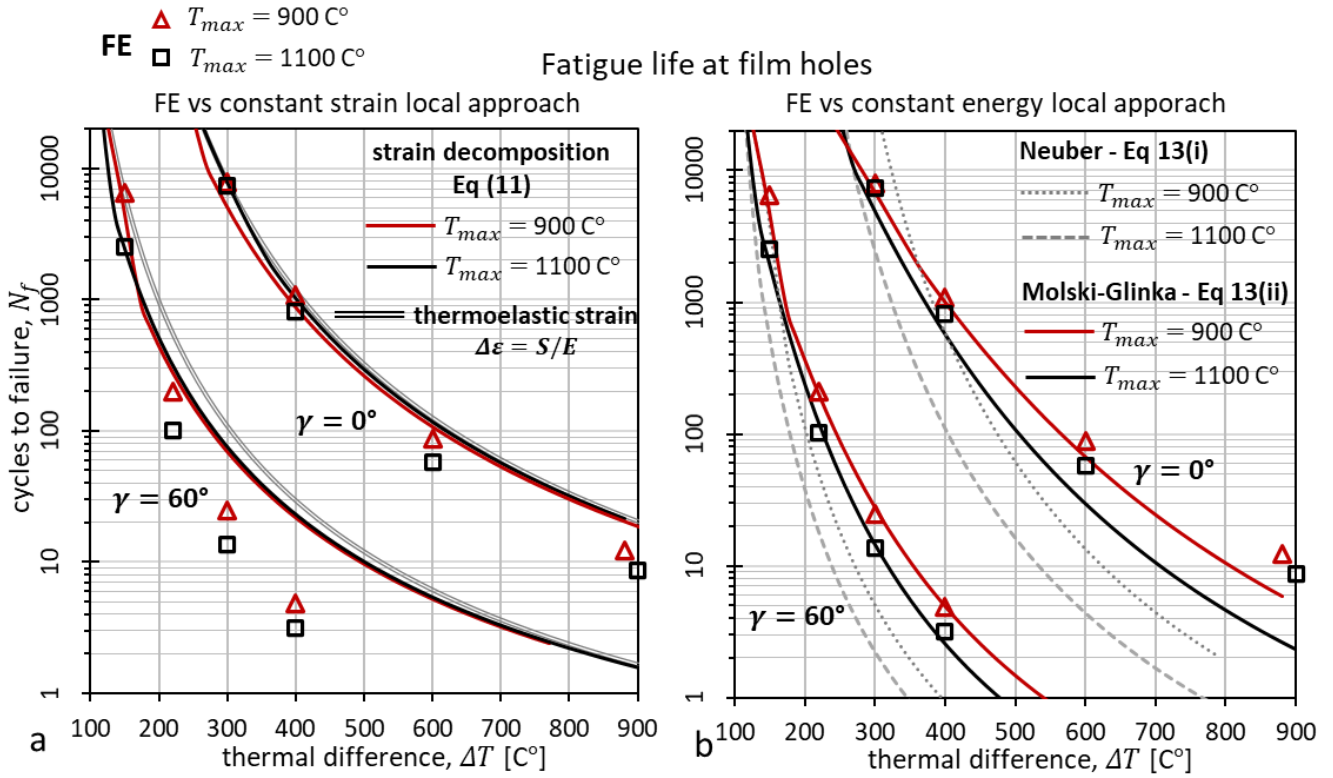


Figure 9. Fatigue life results for the critical film hole location based on inelastic FE cyclic analysis and the local strain approaches, for the transverse  $\gamma = 0^\circ$  and inclined  $\gamma = 60^\circ$  holes at two maximum temperature levels  $T_{max} = 1100\text{ C}^\circ$  and  $T_{max} = 900\text{ C}^\circ$ . (a) Comparison between FE and the local approach based on constant strain. (b) Comparison between FE and the local approach based on the non-incremental Neuber and Molski-Glinka rules for the elastoplastic strain on heat-up (and the creep dwell strain).

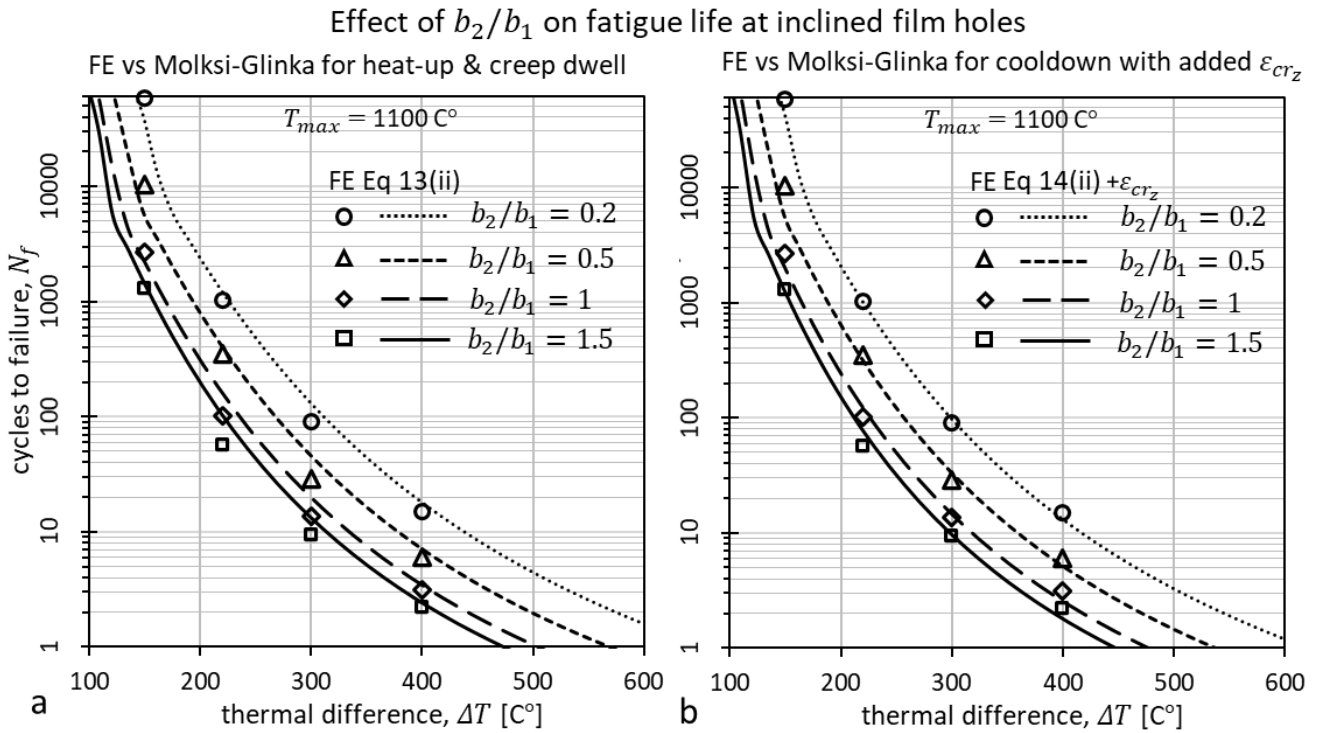


Figure 10. Fatigue life results for the critical location of the inclined hole  $\gamma = 60^\circ$  at  $T_{max} = 1100\text{ C}^\circ$ , as a function of layer thickness ratio,  $b_2/b_1$ . (a) Comparison between FE cyclic analysis and the Molski-Glinka scheme for the elastoplastic strain on heat-up (and the creep dwell strain). (b) Comparison between FE and the Molski-Glinka scheme for the elastoplastic strain on cool-down with the creep strain,  $\epsilon_{crz}$ , correction.

## 5 Discussion

Our fatigue results indicate when film holes are not inclined, i.e.  $\gamma = 0^\circ$ , the cycles to failure,  $N_f$ , for  $\Delta T < 300^\circ\text{C}$ , exceed the typical range, 1000 – 10000, for turbine blade components (Fig 9). However, the life of inclined holes ( $\gamma = 60^\circ$ ) lies within the very low cycle fatigue regime, which is consistent with experimental results for similar hole configurations where fatigue cracks initiated after 100 – 200 loading cycles [21, 41]. This suggests that the cooling benefit of using an extreme inclination  $\gamma = 60^\circ$  should generally be examined carefully in design [6] and that care must be taken to reduce thermal stresses both locally and globally/nominally. An important global effect shown in Fig 10 is that reducing the cool layer thickness of the PDL system offers substantial benefits in life. In terms of local effects, modifying the elliptical shape of the outer hole rim has been shown to reduce remarkably the maximum stress concentration factor (SCF) and thus has been suggested for consideration in design [14]. The hole size, its orientation and its positioning with respect to the pedestals can also help reduce the SCF [14]. Pedestal spacing is an additional global geometric parameter, which although it does not appear in our thermoelastic stress expression (Eq (5)), its effect is captured within the value of the SCF, as the value carries the influence of hole-hole and hole-pedestal interactions. We have indicated that minimizing pedestal spacing maximizes these interactions, and thus reduces the SCF [14]. Our current results demonstrate that the actual benefit of all the above recommendations to fatigue life can be quantified in a straightforward manner, i.e. by combining thermoelastic FE analysis with the local strain approach.

Nevertheless, in many cases, geometry-stress relationships based on maximum principal stress and/or von Mises stress may not suffice to draw definite conclusions on fatigue performance. For example, in single crystal systems used in nickel-based turbine blades [19], fatigue is largely driven by the activation of slip along critical crystallographic planes [8, 27, 42]. In such cases, an assessment based on critical shear stress-strain values, e.g. critical resolved shear stress (CRSS) of the stress field, is essential [43, 44], particularly for configurations with narrow hole-hole distances [45]. This study focuses on the establishing the link between an elastic analysis and a cyclic plasticity-creep analysis. It also provides an understanding of the critical structural and material inelastic phenomena in DPL systems and builds a framework within which anisotropic material effects can be introduced in later stages of design. We may anticipate that the main implications of thermal loading, the critical role of film cooling hole geometry, and the role of cool layer thickness shown here will also be relevant for anisotropic systems. However, the thermo-elastic stress range, the critical local inelastic cycle and the fatigue life results are expected to change. The effect of temperature and orientation dependence of thermal, elastic and plastic properties [8, 33] on the above characteristics will also need consideration in later design stages. In this paper, the variation of  $E$ ,  $\alpha$ ,  $\nu$ , and  $k$ , with temperature has been neglected in order to provide clear understanding of the phenomena occurring during heat-up and cool-down. The effect of temperature dependency of  $E$ ,  $\alpha$ ,  $\nu$  on thermoelastic stresses is evaluated in a later study [46]. The overall role of  $k$  is expected to be less significant for this application, since here we are concerned with thin layers. Moreover, although the temperature dependency of  $k$  can influence the local thermoelastic stress path over a cycle, this is likely to be irrelevant to the low cycle fatigue process, since the latter usually depends primarily on the conditions at the extremes of the cycle [8].

Our recommendations so far, are based on a fixed temperature field, by assuming that geometric modifications do not alter the cooling effectiveness of the system. The design task is to simultaneously minimise thermal stresses and the heat flux into the metal. For this, fatigue life should be calculated for the actual temperature field that is developed when critical features are modified i.e. the film hole shape and the cool layer thickness. This implies that the minimisation of stresses through the geometry should be performed in conjunction with heat transfer analysis and/or CFD simulations of coolant flow through the system. Particularly in new geometries, the potential effect of second order approximations of the temperature field [17] should also be evaluated thermo-

elastically and inelastically. This will verify whether or not the idealised temperature field employed here is a valid approximation for predicting fatigue in PDL systems. This aspect is explored in a later study [32]. Transient temperature effects can also prove significant, in the sense that out-of-phase variation of  $T_{max}$  and  $T_{min}$  (denoted in Fig 1b) can induce negative thermal gradients through the hot layer i.e. thermal up-socks and down-socks [18], leading to complex thermoelastic stress histories at the critical film hole location and therefore different local inelastic cycles. Our incremental local strain approach is a valuable tool for exploring these effects.

Constitutive laws that capture a wider range of material phenomena is also a critical aspect [47]. More elaborate creep laws for stress relaxation are considered a second priority here compared to cyclic plasticity laws, as we have indicated that film holes mainly suffer from severe time independent plasticity due to the extreme SCF = 3.85 and the drastic reduction of yield stress at very high temperatures; note, however, that for low  $\Delta T$ , and for the extreme max temperature of 1100 °C the creep dwell strain can be significant and that dwell periods longer than the one assumed here (1h) may increase their significance. Although plastic hardening/softening is ignored here in order to provide a clear and comprehensive view of the structural integrity issues in PDL systems, these processes can prove essential for characterising and predicting the details of the cyclic response of the system, locally and globally [47].

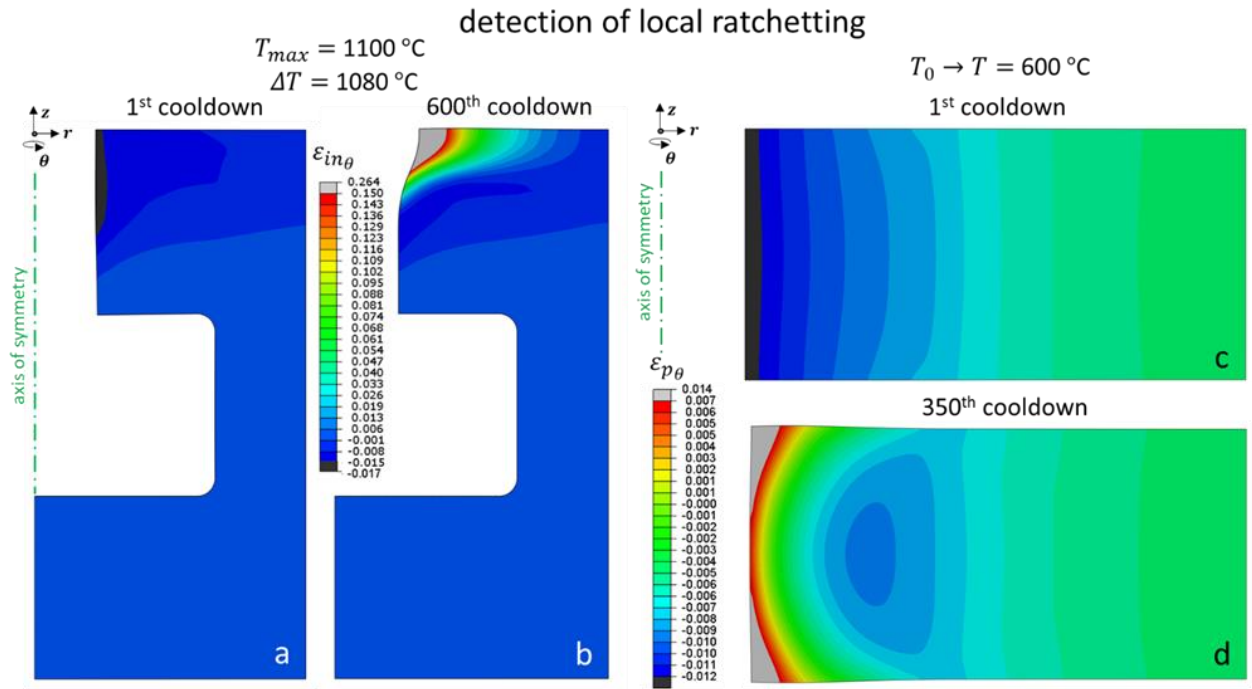


Figure 11. Detection of local ratchetting at the free surface of holes. (a) Plastic strain field in the hoop direction during the first cooldown of the axisymmetric double layer model of Fig 1d, for the elastoplastic-creep material and thermal difference,  $\Delta T$ , across the outer layer. (b) Evolved plastic strain field on cooldown after 600 cycles. (c) Plastic strain field in the hoop direction during the first cooldown of a simplified axisymmetric hole-plate (with constrained external plate radius) under uniform temperature increase and an elastic-perfectly plastic material with temperature independent yield stress (and no creep). (d) Evolved plastic strain during cooldown after 350 cycles.

These additional effects can also influence the ratchet (incremental deformation) phenomenon identified for the inelastic cycles of Fig 7a-b. We provide evidence of this phenomenon in Fig 11, by highlighting how the plastic strain field,  $\epsilon_{p\theta}$ , is modified between the first cooldown and the 600<sup>th</sup> cooldown. Figs 11a-b show the extreme increase of  $\epsilon_{p\theta}$  at the critical hole location, whereas Figs 11c-d are used to show that the ratchet mechanism also occurs in a simpler axisymmetric hole-plate model (with constrained external plate radius), loaded by a uniform temperature difference, and using

an elastic-perfectly plastic material model with temperature independent yield stress (and no creep). Through rigorous FE analysis we have indicated that the mechanism occurs when the critical hole location undergoes reverse plasticity and results in a gradually increase in the distortion of the rim with increasing number of cycles. The presence of a local ratchet mechanism in the absence of mechanical loading has been previously discussed for severe thermal loading situations [18, 48]. Simultaneously, however, studies also support that the FE numerical scheme itself, along with the use of perfect plasticity, can be responsible for the presence of a small ratchet strain per cycle (such as the one here) in the inelastic solution [49]. This suggests that the local ratchet mechanism shown in Fig 11 for pure thermal loading may not in practise compromise the structural integrity of the system. Instead, fatigue failure remains the primary concern.

On the other hand, when thermal loading is combined with mechanical loading, global incremental collapse mechanisms (ratcheting) can be activated [49], and therefore both ratchetting and fatigue should be evaluated. Depending on the component and the application in which the PDL system is used, mechanical/primary stresses can be as important as thermal/secondary stresses. For instance, in gas turbine blades for aeroengines, mechanical loading is severe as it involves tensile centrifugal stresses arising from the steady state rotation of the blade [50], inertial-bending stresses due to the engine acceleration/deceleration [51] as well as gas bending stresses [52]. Generally, the combination of thermal-mechanical loading increases remarkably the complexity of the inelastic response [49], since ratcheting in particular can be highly sensitive to the details of the sequencing of the mechanical and thermal loading histories [53]. Before evaluating the interaction of fatigue and ratchetting, elastic analysis of combined thermal-mechanical loading needs to be performed, particularly for the new PDL systems studied here, where a number of geometric and material effects can arise; this is addressed in a later study [32].

The strategy adopted in this paper, is to concentrate on thermal loading together with a simple material model, with the purpose of providing a framework for studying the behaviour for more complex material models and loading conditions. Simultaneously, we have used a simple fatigue life prediction scheme that doesn't take into account damage that accumulates during combinations of different load cases [54]. Our fatigue life results based on Eq (15) primarily focus on comparing the cyclic strain range predictions between different local strain approaches and detailed FE calculations, with the objective of identifying: suitable approximate methods of determining the cyclic response and its implications for fatigue failure; the effect of thermal cycling on the integrity of PDL systems; and the importance of geometric parameters such as hole inclination and cool wall thickness. The insights gained from this study will allow us to evaluate the sensitivity of the response to the details of the material constitutive model and to evaluate the effect of the full representative thermo-mechanical loading histories on the component behaviour and damage accumulation under a sequence of different flight conditions [54].

## 6 Conclusions

We have investigated thermal stresses and their effects on material creep-plasticity and eventual fatigue failure in new porous double layer (PDL) cooling systems. These systems will allow further increase of gas temperatures in future gas turbines and hypersonic vehicles. The combination of a large stress concentration factor  $SCF = 3.85$  at film holes inclined by  $60^\circ$ , with the considerable thermal stresses induced by the thermal difference between the two layers, is shown to generate excessive local stresses and therefore severe cyclic plasticity.

By using a single SCF value from thermoelastic FE analysis and a local strain approach, the prediction of the local cyclic strain range that leads to fatigue is close to that determined from inelastic FE cyclic solutions. The Molski-Glinka scheme generally gives more accurate and less conservative predictions than Nueber's scheme, while the accuracy of both degrades for film holes that run perpendicular to the surface, where low values of  $SCF = 1.85$  apply.

The local inelastic cycle for inclined holes of 60° involves excessive plastic strains, due to the large SCF combined with the drastic reduction of yield stress at temperatures of 1100 °C for CMSX-4 alloys. Consequently, compressive creep plays a less important role in failure compared to reverse plasticity. The very large local strain ranges are predicted to cause fatigue crack initiation at a very low number of cycles. Therefore, PDL systems can meet typical fatigue life requirements for engine components only if critical geometric features are optimized, such as the film hole shape and the layer thickness ratio. Ratcheting at film holes that are found to occur only under pure thermal loading, impose an additional concern in design. Design innovation can benefit from using more elaborate plastic laws, both in FE analysis and in the incremental local strain methods of Neuber and Molski-Glinka.

Our research develops a basis for integrating PDL systems in future engines to address the timely need for cheaper, greener air transport.

## Acknowledgements

The authors acknowledge Dr Michail Malikoutsakis for useful discussions. The work was supported by EPSRC programme grant EP/P000878/1.

## Data availability statement

The raw/processed data required to reproduce these findings cannot be shared at this time as the data also forms part of an ongoing study.

## References

1. Sengupta, A., et al., *Tensile behavior of a new single-crystal nickel-based superalloy (CMSX-4) at room and elevated temperatures*. Journal of materials engineering and performance, 1994. 3(1): p. 73-81.
2. Nathal, M., et al., *Stress relaxation behavior in single crystal superalloys*. Materials Science and Engineering: A, 2015. 640: p. 295-304.
3. Padture, N.P., M. Gell, and E.H. Jordan, *Thermal barrier coatings for gas-turbine engine applications*. Science, 2002. 296(5566): p. 280-284.
4. Choi, J., et al., *Thermo-mechanical fatigue characteristics of CMSX-4 applied to the high-pressure turbine first-stage single-crystal rotor blade*. Journal of Mechanical Science and Technology, 2020. 34(5): p. 1855-1862.
5. Krewinkel, R., *A review of gas turbine effusion cooling studies*. International Journal of Heat and Mass Transfer, 2013. 66: p. 706-722.
6. Zhang, H., et al., *Effects of compound angle on film cooling effectiveness considering endwall lateral pressure gradient*. Aerospace Science and Technology, 2020: p. 105923.
7. Murray, A.V., et al., *High Resolution Experimental and Computational Methods for Modelling Multiple Row Effusion Cooling Performance*. International Journal of Turbomachinery, Propulsion and Power, 2018. 3(1): p. 4.
8. Reed, R.C., *The superalloys: fundamentals and applications*. 2008: Cambridge university press.
9. Broomfield, R.W., et al., *Development and turbine engine performance of three advanced rhenium containing superalloys for single crystal and directionally solidified blades and vanes*. 1998.
10. Li, W., et al., *Large eddy simulation of compound angle hole film cooling with hole length-to-diameter ratio and internal crossflow orientation effects*. International Journal of Thermal Sciences, 2017. 121: p. 410-423.
11. Ngetich, G.C., et al., *A three-dimensional conjugate approach for analyzing a double-walled effusion-cooled turbine blade*. Journal of Turbomachinery, 2019. 141(1).



12. Murray, A.V., *Advanced gas turbine cooling: double-wall turbine cooling technologies in turbine NGV/blade applications*. 2019, University of Oxford.
13. Cerminara, A., R. Deiterding, and N.D. Sandham, *Transpiration cooling using porous material for hypersonic applications*. *Convective Heat Transfer in Porous Media*, 2019: p. 263.
14. Skamniotis, C. and A.C. Cocks, *Designing against severe effusion hole stresses in double wall transpiration systems for high temperature applications*. To appear, 2021.
15. Skamniotis, C. and A.C. Cocks, *Minimising stresses in double wall transpiration cooled components for high temperature applications*. *International Journal of Mechanical Sciences*, 2020. 189: p. 105983.
16. Skamniotis, C.G. and A.C. Cocks, *2D and 3D thermoelastic phenomena in double wall transpiration cooling systems for gas turbine blades and hypersonic flight*. *Aerospace Science and Technology*, 2021: p. 106610.
17. Elmukashfi, E., et al., *Analysis of the Thermomechanical Stresses in Double-Wall Effusion Cooled Systems*. *Journal of Turbomachinery*, 2020. 142(5).
18. Karadeniz, S. and A. Ponter, *The influence of transient thermal loading on the Bree plate; A simplified method of analysis*. *Nuclear Engineering and Design*, 1984. 80(3): p. 359-374.
19. Mücke, R. and O.-E. Bernhardt, *A constitutive model for anisotropic materials based on Neuber's rule*. *Computer methods in applied mechanics and engineering*, 2003. 192(37-38): p. 4237-4255.
20. Chen, H. and A.R. Ponter, *A simplified creep-reverse plasticity solution method for bodies subjected to cyclic loading*. *European Journal of Mechanics-A/Solids*, 2004. 23(4): p. 561-577.
21. Zhou, Z.-J., et al., *Effect of skew angle of holes on the thermal fatigue behavior of a Ni-based single crystal superalloy*. *Acta Metallurgica Sinica (English Letters)*, 2017. 30(2): p. 185-192.
22. Zamiri, A., S.J. You, and J.T. Chung, *Large eddy simulation of unsteady turbulent flow structures and film-cooling effectiveness in a laidback fan-shaped hole*. *Aerospace Science and Technology*, 2020: p. 105793.
23. Neuber, H., *Theory of stress concentration for shear-strained prismatical bodies with arbitrary nonlinear stress-strain law*. 1961.
24. Molski, K. and G. Glinka, *A method of elastic-plastic stress and strain calculation at a notch root*. *Materials Science and Engineering*, 1981. 50(1): p. 93-100.
25. Zhu, S.-P., et al., *A combined high and low cycle fatigue model for life prediction of turbine blades*. *Materials*, 2017. 10(7): p. 698.
26. Chen, L., Y. Liu, and L. Xie, *Power-exponent function model for low-cycle fatigue life prediction and its applications—Part II: Life prediction of turbine blades under creep-fatigue interaction*. *International journal of fatigue*, 2007. 29(1): p. 10-19.
27. Cunha, F., M. Dahmer, and M. Chyu. *Thermal-Mechanical Life Prediction System for Anisotropic Turbine Components*. in *Turbo Expo: Power for Land, Sea, and Air*. 2005.
28. Banaszkiwicz, M., *Numerical investigations of crack initiation in impulse steam turbine rotors subject to thermo-mechanical fatigue*. *Applied Thermal Engineering*, 2018. 138: p. 761-773.
29. Chen, H. and A.R. Ponter, *Linear Matching Method on the evaluation of plastic and creep behaviours for bodies subjected to cyclic thermal and mechanical loading*. *International Journal for Numerical Methods in Engineering*, 2006. 68(1): p. 13-32.
30. Abaqus, V., *6.14 Documentation*. Dassault Systemes Simulia Corporation, 2014. 651: p. 6.2.
31. Murray, A.V., P.T. Ireland, and A.J. Rawlinson. *An Integrated Conjugate Computational Approach for Evaluating the Aerothermal and Thermomechanical Performance of Double-Wall Effusion Cooled Systems*. in *ASME Turbo Expo 2017: Turbomachinery Technical Conference and Exposition*. 2017. American Society of Mechanical Engineers Digital Collection.
32. Skamniotis, C. and A.C. Cocks, *Multiscale analysis of thermomechanical stresses in double wall transpiration cooling systems for gas turbine blades*. To appear, 2021.
33. Dye, D., et al. *Welding of Single Crystal Superalloy CMSX-4: Experiments and Modeling*. in *Superalloys 2004 (Tenth International Symposium)*. 2004.

34. Ince, A., G. Glinka, and A. Buczynski, *Computational modeling of multiaxial elasto-plastic stress-strain response for notched components under non-proportional loading*. International Journal of Fatigue, 2014. 62: p. 42-52.
35. Scholz, A., et al., *Modeling of mechanical properties of alloy CMSX-4*. Materials Science and Engineering: A, 2009. 510: p. 278-283.
36. Coffin Jr, L.F., *A study of the effects of cyclic thermal stresses on a ductile metal*. Transactions of the American Society of Mechanical Engineers, New York, 1954. 76: p. 931-950.
37. Basquin, O. *The exponential law of endurance tests*. in *Proc Am Soc Test Mater*. 1910.
38. Karadeniz, S., A. Ponter, and K.J.J.o.p.v.t. Carter, *The plastic ratcheting of thin cylindrical shells subjected to axisymmetric thermal and mechanical loading*. 1987. 109(4): p. 387-393.
39. Visvanatha, S., P. Straznicky, and R. Hewitt, *Influence of strain estimation methods on life predictions using the local strain approach*. International Journal of Fatigue, 2000. 22(8): p. 675-681.
40. Hoffmann, M. and T. Seeger, *Stress-strain analysis and life predictions of a notched shaft under multiaxial loading*. Multiaxial Fatigue: Analysis and Experiments, AE, 1989. 14: p. 81-99.
41. Gemma, A. and J. Phillips, *The application of fracture mechanics to life prediction of cooling hole configurations in thermal-mechanical fatigue*. Engineering Fracture Mechanics, 1977. 9(1): p. 25-36.
42. Li, Z., et al., *In-situ observation of crack initiation and propagation in Ni-based superalloy with film cooling holes during tensile test*. Journal of Alloys and Compounds, 2019. 793: p. 65-76.
43. Wen, Z., et al., *A combined CP theory and TCD for predicting fatigue lifetime in single-crystal superalloy plates with film cooling holes*. International Journal of Fatigue, 2018. 111: p. 243-255.
44. Wen, Z., et al., *Prediction method for creep life of thin-wall specimen with film cooling holes in Ni-based single-crystal superalloy*. International Journal of Mechanical Sciences, 2018. 141: p. 276-289.
45. Wang, J., et al., *The inter-hole interference on creep deformation behavior of nickel-based single crystal specimen with film-cooling holes*. International Journal of Mechanical Sciences, 2019. 163: p. 105090.
46. Skamniotis, C. and A.C. Cocks, *Thermal-centrifugal stresses in double wall transpiration cooled components with curvature and temperature dependent thermoelastic properties*. To appear, 2021.
47. XiaoAn, H., et al., *Viscoplastic analysis method of an aeroengine turbine blade subjected to transient thermo-mechanical loading*. International Journal of Mechanical Sciences, 2019. 152: p. 247-256.
48. Cocks, A. and A. Ponter, *The plastic behaviour of components subjected to constant primary stresses and cyclic secondary strains*. The Journal of Strain Analysis for Engineering Design, 1985. 20(1): p. 7-14.
49. Ma, Z., et al., *A unified direct method for ratchet and fatigue analysis of structures subjected to arbitrary cyclic thermal-mechanical load histories*. International Journal of Mechanical Sciences, 2021. 194: p. 106190.
50. Kauss, O., et al., *Structural analysis of gas turbine blades made of Mo-Si-B under transient thermo-mechanical loads*. Computational Materials Science, 2019. 165: p. 129-136.
51. Sadowski, T. and P. Golewski, *Detection and numerical analysis of the most efforted places in turbine blades under real working conditions*. Computational Materials Science, 2012. 64: p. 285-288.
52. Poursaeidi, E., et al., *Effects of natural frequencies on the failure of R1 compressor blades*. Engineering Failure Analysis, 2012. 25: p. 304-315.
53. Chen, H. and A.R. Ponter, *Shakedown and limit analyses for 3-D structures using the linear matching method*. International Journal of Pressure Vessels and Piping, 2001. 78(6): p. 443-451.

54. Sun, Q., H.-N. Dui, and X.-L. Fan, *A statistically consistent fatigue damage model based on Miner's rule*. International Journal of Fatigue, 2014. 69: p. 16-21.